



NTNU – Trondheim
Norwegian University of
Science and Technology

Modeling and Testing of Impact Damage in Composite Pressure Vessels

Martin Welle Skaar

Master of Science in Mechanical Engineering

Submission date: June 2015

Supervisor: Andreas Echtermeyer, IPM

Norwegian University of Science and Technology
Department of Engineering Design and Materials

Abstract

Composite pressure vessels are becoming widely used for transporting gas, lately also hydrogen. In order to enable extensive use of the pressure vessels, it is critical to ensure their societal acceptance, and thus safety under transportation. Being able to judge the damage of an impacted pressure vessels is one important aspect from a safety and economical point of view. The lack of knowledge about the behaviour of damaged pressure vessels results in needlessly discarding damaged vessels with acceptable levels of damage.

This thesis considers impact damage on glass fibre reinforced polymer pipes, produced by filament winding. Pipe specimens were subjected to well-defined impacts for two energy levels and the damage was reproduced numerically. Interlaminar damage was modelled by cohesive elements between composite layers. Intralaminar damage was modelled by the Hashin failure criterion on continuum shell elements.

Experimental impacts produced unexpected highly asymmetrical delaminations. These delaminations were reproducible in shape and size for all specimens. The numerical model predicted the asymmetrical delaminations within the scatter of the experimental results for both energy levels tested. By studying the interlaminar behaviour of the delamination in the model, the buckling mode of the pipe was found to determine the direction of delamination. The intralaminar damage (fibre failure and matrix cracking) was inconsistent for the experimental impacts. Results ranged from no fibre damage, to large cracks with total fibre failure. Both the location and extent of fibre damage for the heavily damaged specimen could be reproduced numerically. Material properties that are critical for the modelling were identified.

Samandrag

Trykktankar i kompositt vert i aukande grad nytta til å transportere gass, i det siste også hydrogen. For å tillate utstrekt bruk av tankane er det kritisk å sikre deira samfunnsmessige aksept, og derfor tryggleik under transport. Å vere i stand til å døme skada på ein støytskada tank er veldig viktig, både med tanke på tryggleik og økonomi. Manglande kunnskap om oppførselen til skada tankar resulterer i unødvendig forkasting av tankar som ikkje er kritisk skadd.

Denne avhandlinga tek for seg støytskadar på glasfiberforsterka polymerrøyr, produsert ved vikling. Røyrprøvar vart utsett for veldefinerte støyt ved to energinivå, skadane vart så gjenskapte numerisk. Interlaminær skade vart modellert ved cohesive elements mellom komposittlaga. Intralaminær skade vart modelert ved bruk av Hashin feilkriterie på continuum shell elements.

Eksperimentelle støyt skapte uventa asymmetriske delamineringar. Desse var reproduserbare i størrelse og form for alle prøvene. Den numeriske modellen spådde den asymmetriske delamineringa, innanfor spreinga av dei eksperimentelle resultatata, for begge energinivåa som vart testa. Gjennom å studere den interlaminære oppførselen i modellen, vart bukingsmoden til røyret funne å avgjere retninga til delamineringa. Den intralaminære skada (fibersvikt og matriseprekkar) var ikkje konsekvent for dei ulike prøvane. Resultata varierte frå inga fiberskade, til store sprekkjer med total fibersvikt. Både plassering og utbreiing av skada for den svært skadde prøva lot seg produsere numerisk. Materialeigenskapar som er kritiske for modellen vart identifisert.

Preface

This thesis has been submitted in fulfilment of the Master of Science degree at the Norwegian University of Science and Technology, under the supervision of Professor *Andreas T. Echtermeyer* and Associate Professor *Nils P. Vedvik*.

The present work was performed at the Department of Engineering Design and Materials, Faculty of Engineering Science and Technology (NTNU).

Acknowledgments

I would like to thank both my supervisors, Professor *Andreas T. Echtermeyer* and Assoc. Professor *Nils P. Vedvik* for valuable input and guidance during the writing of this thesis. I would also like to thank *Carl M. Midtbø* for all help with the practical work on this thesis.

A special thanks goes to the drift at room 230, who made life more interesting for both myself and the cleaning staff during my last year at NTNU.

Table of Contents

Abstract	
Samandrag	
Preface	iii
Acknowledgments	iv
Table of Contents	iv
List of Tables	vii
List of Figures	ix
1 Introduction	1
2 Theory	3
2.1 Hashin failure criterion	3
2.2 Cohesive elements	5
3 Experimental method	9
3.1 Material production	9
3.2 Pipe quality assessment	10
3.3 Experimental setup	13
3.3.1 Damage creation	13
3.3.2 Evaluation of elastic response	15
4 Numerical method	17

4.1	Material parameters	18
4.1.1	Material stiffness parameters	18
4.1.2	Delamination parameters	18
4.1.3	Hashin damage parameters	19
4.1.4	Material data table	21
4.2	Model buildup	22
4.3	Mesh convergence analysis	27
4.4	Model stiffness evaluation	32
4.5	Choosing damage predictors	33
4.5.1	Delamination damage	33
4.5.2	Intralaminar damage	33
5	Results	35
5.1	Experimental impact damage	35
5.2	Numerical damage	40
5.2.1	Interlayer damage	40
5.2.2	Delamination evolution	42
5.2.3	Effect on Hashin damage on delamination	48
5.2.4	Delamination sensitivity analysis	49
5.2.5	Intralaminar damage	53
6	Discussion	57
7	Conclusion	63
8	Further work	65
	Bibliography	65
	Appendix A: Burst pressure testing	69
	Appendix B: Winding procedure	72
	HMS and signed problem text	76

List of Tables

3.1	Equipment and materials used for filament winding.	10
3.2	Layer thickness in pipe.	12
3.3	Material weights and V_f found through burn-off.	12
4.1	Material parameters and their values for FE-model.	21
4.2	Overview of model properties.	25
4.3	Effect of mesh size in damage region on calculation time.	30
5.1	Average size of experimental delaminations.	39
5.2	Size of numerical delaminations for both impact heights.	41

List of Figures

2.1	Relationship between G_C and equivalent displacement for Hashin damage.	4
2.2	Relationship between traction force and separation.	6
2.3	Strain energy release as function of separation for cohesive elements.	7
3.1	First 90° layer of a pipe being applied to mandrel.	9
3.2	Coordinate system used in pipe layers.	10
3.3	View directions and samples for microscopy inspection.	11
3.4	Microvoids in outer hoop layer.	11
3.5	Fibres of a sample after burn-off.	12
3.6	Pipe, impactor and cradle with dimensions.	13
3.7	Fibre failure estimation through burn-off testing.	14
3.8	Burn-off of seemingly undamaged fibres.	14
3.9	Pipe being impacted while strain is continuously measured.	15
4.1	Microscopy of pipe.	18
4.2	Fracture planes.	20
4.3	Overview of the FE-model.	22
4.4	Exploded view of the damage zone.	23
4.5	Exploded view of general region.	24
4.6	Example of model during impact.	26
4.7	Convergence with refinement of general region mesh.	27
4.8	Convergence with refinement of damage region mesh. Without Hashin damage and delamination.	28
4.9	Impact of mesh density on Hashin damage.	29
4.10	Convergence with refinement of cohesive layers.	30
4.11	Impact of mesh density on delamination	31
4.12	Correlation between experimental and numerical strain during impact.	32

4.13	Border between damaged and undamaged cohesive elements.	33
5.1	Damage from 1.0 m (28.45 J) impacts.	36
5.2	Damage from 1.5 m (42.67 J) impacts.	37
5.3	Internal matrix damage from 1m and 1.5m impacts.	38
5.4	Numerical delamination from 1.0 m impact.	40
5.5	Numerical delamination from 1.5m impact.	40
5.6	Evolution of deleted cohesive elements.	42
5.7	View cut of central element arch during impact.	43
5.8	Internal view of delamination, $t \leq 2.4\text{ms}$	44
5.9	Internal view of delamination, $t > 2.4\text{ms}$	45
5.10	Stress distribution in inner cohesive layer.	46
5.11	Stress distribution in inner cohesive layer continued.	47
5.12	Delamination in inner and outer cohesive layer with no Hashin damage.	48
5.13	Delamination in inner and outer cohesive layer with Hashin damage.	48
5.14	Delamination in inner and outer cohesive layer for the base model.	49
5.15	Delamination in inner and outer cohesive layer with adjusted G_{IC}	50
5.16	Delamination in inner and outer cohesive layer with adjusted G_{IIC}/G_{IIIC}	50
5.17	Delamination in inner and outer cohesive layer with adjusted tensile and shear failure stresses.	51
5.18	Delamination in inner and outer cohesive layer with adjusted tensile and shear stiffness.	51
5.19	Delamination in inner and outer cohesive layer with adjusted impact location.	52
5.20	Fibre damage envelope due to compression and tension. 1 m impact.	53
5.21	Matrix damage envelope due to compression and tension. 1 m impact.	54
5.22	Strain through section points of top layer during impact.	55
5.23	Stress through section points of top layer during impact.	55
5.24	Tensile and compressive fibre damage through section points of top layer. 1 m impact	56
6.1	Buckling mode simulation of an arch.	58

Introduction

Composite pressure vessels are becoming widely used for transporting gas, lately also hydrogen. In order to enable extensive use of the pressure vessels, it is of primary importance to ensure their societal acceptance, and thus safety under transportation must be secured. In particular, the knowledge on composite overwrapped pressure vessels' (COPW) behaviour when submitted to mechanical impacts is limited and existing standards are not well-appropriate to composite materials.

It is important to be able to judge the residual strength of damaged pressure vessels. Not only with regards to safety, but also economy, as fully functional vessels must be discarded if the residual strength is unknown. Ultimately, determining the residual strength based on simple damage parameters would be extremely useful. However, due to the complex nature of damage in composite layups, finding such parameters is difficult.

In order to separate critically damaged vessels from vessels with less severe damage, detailed knowledge of how the damaged vessels behave is needed. This includes the behaviour as a vessel is impacted and damage is created, as well as how the damage propagates when the internal pressure is several hundred atmospheres.

Much research has been made in the field of FEM-simulations of composite damage. However, the majority of the articles consider flat plates [1, 2, 3, 4, 5, 6]. Of the many articles concerning impact damage on flat plates, a great deal focused on either delamination or fibre damage alone. None of the articles found by the author considered delaminations that were greatly asymmetrical in nature.

For the GFRP-pipes investigated in this thesis, both the geometry and the production technique is vastly different from the one used in flat plate specimens. This makes it difficult to select proper material parameters, as relevant material tests are hard to come by.

There are some publications concerning damage in filament wound composite pipes [7, 8], but the understanding of the subject is somewhat limited.

This thesis investigates the feasibility of using Hashin's failure criterion on continuum shell elements, combined with cohesive elements to model both matrix and fibre damage, as well as delamination in filament wound composite pipes, using Abaqus. The thesis attempts to build a robust model that can accurately predict complex damage patterns in a timely fashion without the use of complex subroutines. The model accomplishes this by using Hashin's failure criterion for fibre and matrix damage, and discrete layers of cohesive elements for modelling the delamination. To keep calculation time low, the model is separated into a damage region with delamination layers and a fine mesh, and a general region in which delamination cannot occur, and the damage is limited to small degrees of matrix damage. The general region is coarsely meshed, and does not contain any delamination layers. This keeps computational time reasonable, even for the finely meshed model.

The model considered impacts aimed at the apex of the pipes using a spherical impactor tip, which produced a highly asymmetrical damage. Two different energy levels (42.67 J and 28.45 J) were investigated. The impactor had a mass of 2.9 kg, and the drop heights were set at 1 m, and 1.5 m. The experimental damage was investigated, and compared to the numerical damage.

The motivation for the thesis is that a relatively simple model that can predict complex damage, can be used to model the outcome of many different damages. This can then serve as a valuable tool to further the understanding of impact damage. Ideally it is able to accurately predict the extent of damage from various impacts.

2.1 Hashin failure criterion

Damage initiation

Hashin failure model proposed by Hashin in 1980 was used [9] was used to evaluate fibre and matrix damage. This model considers four different damage types: fibre tension, fibre compression, matrix tension, and matrix compression. Damage initiation is predicted by the following equations:

$$F_f^t = \left(\frac{\hat{\sigma}_{11}}{X^T}\right)^2 + \left(\frac{\hat{\tau}_{12}}{S^L}\right)^2, \text{ Fiber tension } \hat{\sigma}_{11} \geq 0 \quad (2.1)$$

$$F_f^c = \left(\frac{\hat{\sigma}_{11}}{X^C}\right)^2, \text{ Fiber compression } \hat{\sigma}_{11} < 0 \quad (2.2)$$

$$F_m^t = \left(\frac{\hat{\sigma}_{22}}{Y^T}\right)^2 + \left(\frac{\hat{\tau}_{12}}{S^L}\right)^2, \text{ Matrix tension } \hat{\sigma}_{22} \geq 0 \quad (2.3)$$

$$F_m^c = \left(\frac{\hat{\sigma}_{22}}{2S^T}\right)^2 + \left[\left(\frac{Y^C}{S^T}\right)^2 - 1\right] \frac{\hat{\sigma}_{22}}{Y^C} + \left(\frac{\hat{\tau}_{12}}{S^L}\right)^2, \text{ Matrix compression } \hat{\sigma}_{22} < 0 \quad (2.4)$$

Where X^T , X^C , Y^T , Y^C , S^L , S^T are the longitudinal tensile and compressive strengths, the transverse tensile and compressive strengths, and the longitudinal and transverse shear strengths, respectively.

Damage evolution

After F_f^t , F_f^c , F_m^t or F_m^c reaches 1 for an integration point, the stiffness of the element will gradually decline. The new stiffness of the element is calculated through the use of

Equation 2.5 and 2.6.

$$\sigma = \mathbf{C}_d \epsilon \quad (2.5)$$

$$\mathbf{C}_d = \frac{1}{D} \begin{bmatrix} (1-d_f)E_1 & (1-d_f)(1-d_m)\nu_{21}E_1 & 0 \\ (1-d_f)(1-d_m)\nu_{12}E_2 & (1-d_m)E_2 & 0 \\ 0 & 0 & (1-d_s)GD \end{bmatrix} \quad (2.6)$$

$$D = 1 - (1-d_f)(1-d_m)\nu_{12}\nu_{21} \quad (2.7)$$

$$d_f = \begin{cases} d_f^t & \text{if } \hat{\sigma}_{11} \geq 0 \\ d_f^c & \text{if } \hat{\sigma}_{11} < 0 \end{cases} \quad (2.8)$$

$$d_m = \begin{cases} d_m^t & \text{if } \hat{\sigma}_{22} \geq 0 \\ d_m^c & \text{if } \hat{\sigma}_{22} < 0 \end{cases}$$

$$d_s = 1 - (1-d_f^t)(1-d_f^c)(1-d_m^t)(1-d_m^c) \quad (2.9)$$

d_f , d_m and d_s are damage variables for the fibre, matrix and shear damage respectively. The rate at which the stiffness decreases with regards to the strain (represented by an equivalent displacement, δ , to alleviate mesh dependency) is defined through energy release rates for each mode (Figure 2.1).

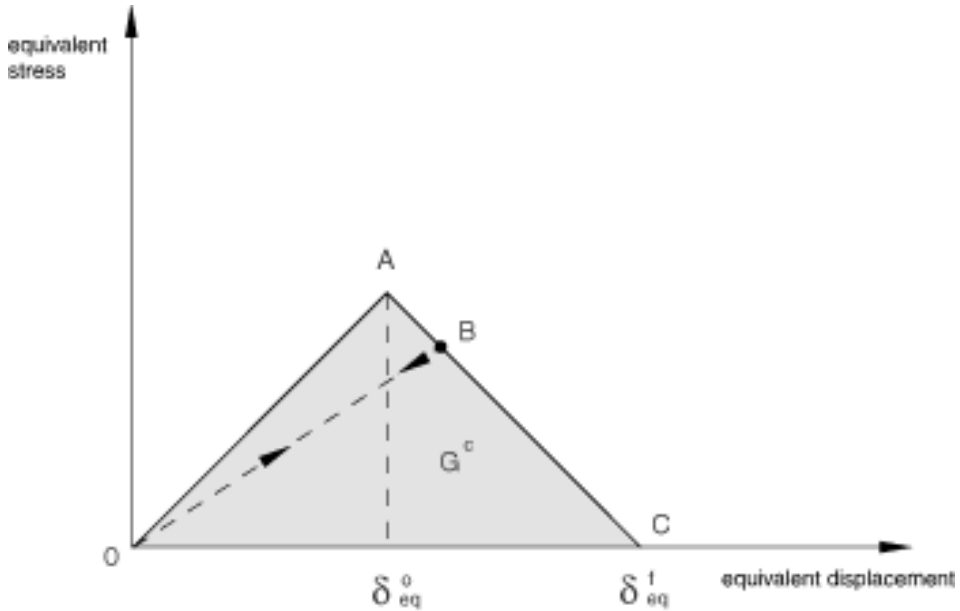


Figure 2.1: Relationship between G_C and equivalent displacement for Hashin damage [10]. Arrows show an exemplified loading path.

As the elements softens, the stresses are redistributed to adjacent elements and the damage evolves. When the damage in an element is total, meaning that $d_f = d_m = d_s = 1$ for all integration points, the element is removed. More details on the implementation of Hashin in Abaqus can be found in the Abaqus User Manual [10].

2.2 Cohesive elements

Cohesive element stiffness

Cohesive elements are special elements integrated in Abaqus to model the behaviour of adhesive joints and interfaces in composites. For this analysis, three dimensional cohesive elements are used (COH3D8). These are assigned a normal stiffness out of plane, E_{nn} , an in plane shear stiffness, E_{ss} and a transverse shear stiffness, E_{tt} . These stiffnesses define the cohesive layer's elastic properties through Equation 2.10 [10].

$$\mathbf{t} = \begin{Bmatrix} t_n \\ t_s \\ t_t \end{Bmatrix} = \begin{bmatrix} E_{nn} & E_{ns} & E_{nt} \\ E_{ns} & E_{ss} & E_{st} \\ E_{nt} & E_{ss} & E_{tt} \end{bmatrix} \begin{Bmatrix} \epsilon_n \\ \epsilon_s \\ \epsilon_t \end{Bmatrix} \quad (2.10)$$

For uncoupled behaviour between the normal and shear components, the off-diagonal terms are set to zero.

Damage initiation

To predict the damage of the cohesive layer, several different damage laws for traction separation exist. These are either strain based, or stress based. In this thesis, a stress based damage criteria is used. The simplest of these criteria is the Maxs criterion. When using this criterion, damage initiates when Equation 2.11 is fulfilled.

$$\max \left\{ \frac{\langle t_n \rangle}{t_n^0}, \frac{t_s}{t_s^0}, \frac{t_t}{t_t^0} \right\} = 1 \quad (2.11)$$

A more advanced approach, which includes the combined damage effects from both normal, transverse shear and in plane shear, is the Quadratic nominal stress criterion:

$$\left\{ \frac{\langle t_n \rangle}{t_n^0} \right\}^2 + \left\{ \frac{t_s}{t_s^0} \right\}^2 + \left\{ \frac{t_t}{t_t^0} \right\}^2 = 1 \quad (2.12)$$

In Equations 2.11 and 2.12, $\langle \rangle$ represents the Macaulay bracket, meaning compressive stresses generate no damage. The quadratic nominal stress criterion is used for damage initiation in the models.

Damage evolution

When the stresses of a cohesive element satisfies equation 2.11 or 2.12, the stiffness of the element starts to diminish as seen in Figure 2.2.

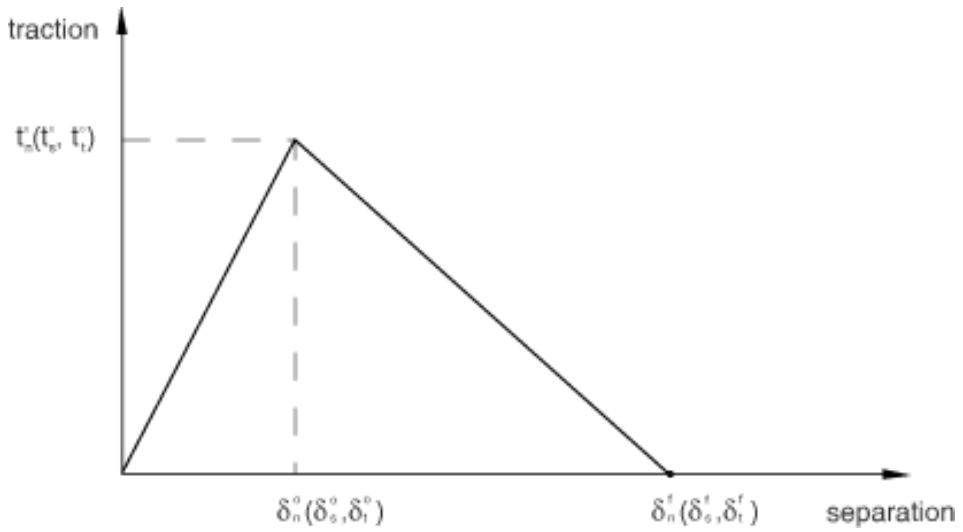


Figure 2.2: Relationship between traction force and separation. Linear softening [10].

The stiffness of the cohesive elements for the normal and shear directions are reduced as shown in Equation 2.13.

$$\begin{aligned}
 t_n &= \begin{cases} (1-D)\bar{t}_n & \text{when } t_n > 0 \\ \bar{t}_n & \text{otherwise} \end{cases} \\
 t_s &= (1-D)\bar{t}_s \\
 t_t &= (1-D)\bar{t}_t
 \end{aligned} \tag{2.13}$$

When evaluating D for a linear softening model, D is found through the use of Equation 2.14.

$$D = \frac{\delta_m^f(\delta_m^{max} - \delta_m^0)}{\delta_m^{max}(\delta_m^f - \delta_m^0)} \tag{2.14}$$

Where δ_m^f is the displacement at zero remaining stiffness, δ_m^{max} is the maximum displacement experienced during the loading history, and δ_m^0 is the displacement at damage initiation.

The rate at which a cohesive element disintegrates can be defined through the strain energy release rate. As depicted in Figure 2.3, the total area represents the total energy released as the element experiences displacements until total failure.

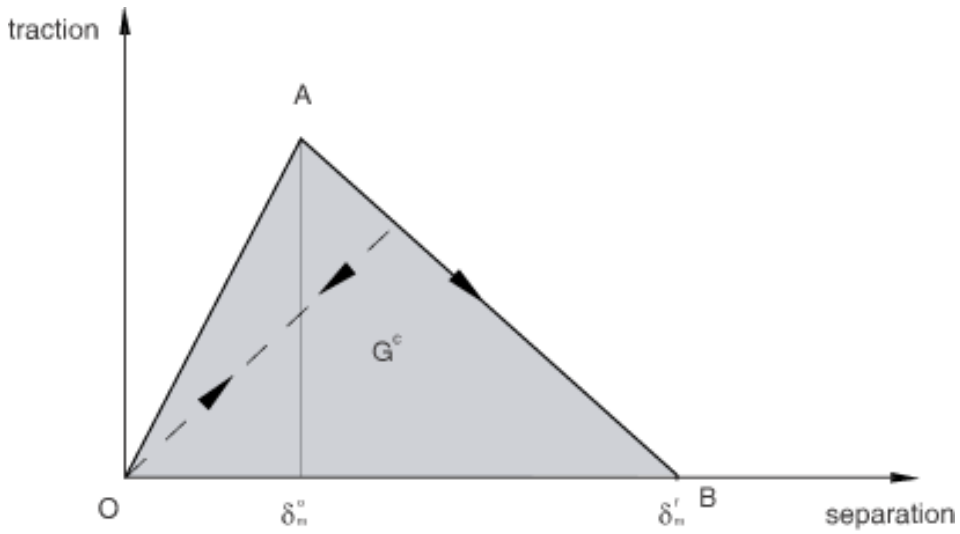


Figure 2.3: The area represents energy released (G^c) as fracture surface is created through the degradation of elements. The arrows indicate load curves [10].

In complex load cases, energy is released through both mode 1, 2 and 3. In this thesis, the two shear mode energy release rates, G_{IIc} and G_{IIIc} are assumed to be equal.

When this is the case, the *Benzeggagh-Kenane* fracture criterion is particularly useful.

This criterion combines the energy released from both normal and shear separation through equation 2.15.

$$G^c = G_n^C + (G_s^C - G_n^C) \left\{ \frac{G_S}{G_T} \right\}^\eta \quad (2.15)$$

Where η is a material parameter which can be evaluated by a Mixed Mode Bending test. G_n^C and G_s^C is the critical energy release rate for normal and shear modes. G_S and G_T is the energy released through shear, and the total energy released.

Cohesive element dimensions

The delamination described by the cohesive elements is highly mesh dependent. According to Turon et al. [11], the required size of the cohesive elements can be determined by Equations 2.16 and 2.17.

$$l_{cz} = \frac{9\pi}{32} E_m \left(\frac{G_c}{(t^0)^2} \right) \quad (2.16)$$

$$l_e = \frac{l_{cz}}{N_e} \quad (2.17)$$

Where l_{cz} is the length of the cohesive zone, E_m is the elastic modulus of the cohesive element, G_c is the fracture toughness and t^0 is the maximum strength of the interface. The length of the individual element (l_e) is determined by the length of the cohesive zone, and the number of elements in the cohesive zone (N_e). The recommended number of elements in the cohesive zone, according to Turon et al. [11] is 3 or 4 elements.

3.1 Material production

The impact tests were carried out on pipes produced by filament winding. The materials and equipment used are presented in Table 3.1. The pipes were wound on a slightly conical mandrel with an external diameter of ≈ 100 mm. A pipe during production is shown in Figure 3.1. All the specimens in this thesis are produced in an identical manner, using the same lay-up.

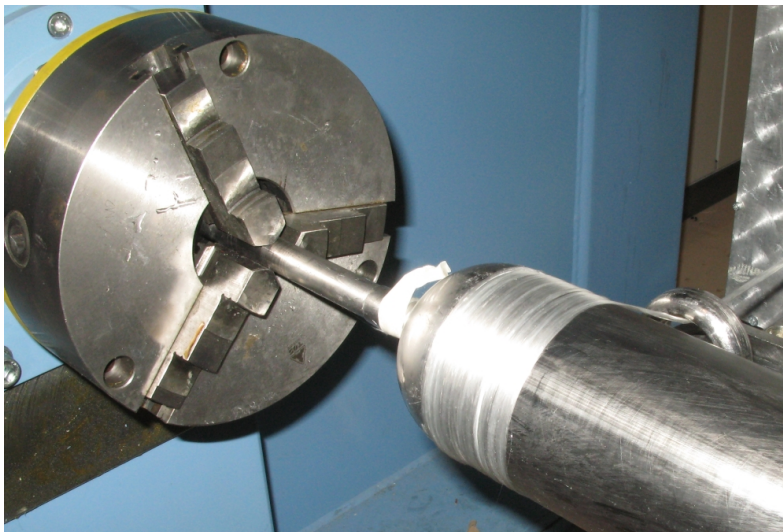


Figure 3.1: First 90° layer of a pipe being applied to mandrel.

A lay-up of $90^\circ/90^\circ/15^\circ/-15^\circ/90^\circ/90^\circ$ was chosen for the pipe. This lay-up has roughly twice the strength in hoop direction as in the longitudinal direction. For internal compression this is a common lay-up, since the hoop strength will be roughly twice the longitudinal strength. This corresponds to stresses in an internally pressurised cylinder. A longitudinal layer of $15^\circ/-15^\circ$ was chosen due to limitations of production method. A minimum angle of the fibre is required to press the fibre against the mandrel, consolidating the laminate. The coordinate system for the layers can be seen in Figure 3.2. Another advantage of the $15^\circ/-15^\circ$ lay-up is that all the crossover points are placed in three distinct regions along the length (crossover points are points where the $\pm 15^\circ$ layers are interwoven). This makes the modelling of the pipe easier as regions where the layers are not interwoven can be chosen for the impacts.

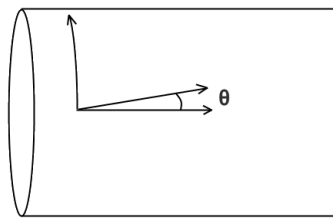


Figure 3.2: Coordinate system used in pipe layers. An angle of 0 degrees corresponds to the longitudinal direction.

Table 3.1: Equipment and materials used for filament winding.

Equipment/Material type	Specific name
Filament winding machine	Microsam MAW 20 LS 4/1
Fibre tensioner for FWM	METS-8
Filament winding software	CNC Winding Commander 8.0
Glass fibre	3B E-CR Glass
Epoxy resin	EPIKOTE Resin MGS RIMR 135
Epoxy hardener	EPIKURE MGS RIMH 134
Slip-coat	FlexZ Z3.0 Slipcoat system
Slip-wax	RELEASE QV5110

3.2 Pipe quality assessment

Microscopy investigations were performed to study the material composition of the pipe in detail. Cuts were made into the material, so the lay-up could be viewed from different angles (Figure 3.3). The cut-outs from Figure 3.3 were used to perform measurements on the layer thickness, in addition to examine the general state of the pipe.

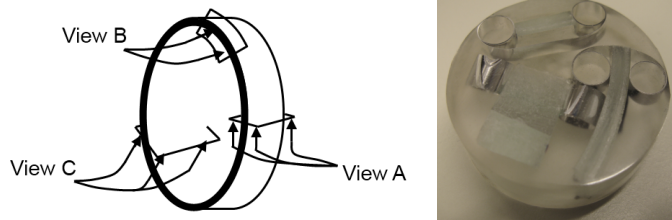


Figure 3.3: View directions and samples for microscopy inspection.

Micro-voids

Since the filament winding technique involves several steps that aerates the epoxy solution, micro-voids are present to a much larger degree than in laminates produced by vacuum infusion. As shown in Figure 3.4, the matrix contained a relatively large amount of micro-voids.

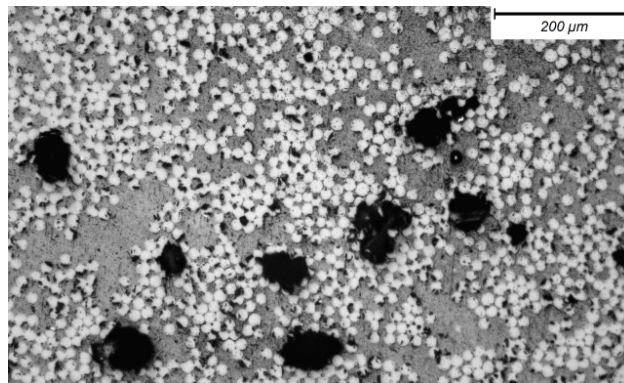


Figure 3.4: Microvoids in outer hoop layer, seen from view A. The black dots are air bubbles trapped in the matrix during production.

Photoshop and pixel count on black pixels was used to calculate the void percentage in the pipes. Void percentage average was found to be 6.25 %. These voids are present to a much larger degree in filament wound pipes than in vacuum infused plates, and are likely to serve as prime initiation points for damage development.

The layer thickness average of all layers was also estimated. The tabulated results in Table 3.2 are used in the FE-model.

Table 3.2: Layer thickness in pipe. Layer numbering starts at inner layer.

Layer nr.	Orientation	Thickness
1+2	90°	0.759 mm
3+4	+15°/-15°	1.013 mm
5+6	90°	0.759 mm

Fibre fraction through burn-off testing

Burn-off tests were conducted to estimate the volume fraction of fibre (V_f). By measuring the weight of the sample before and after burning, the weight of both the fibres and the matrix was determined. The relative volume of components were calculated through their respective densities. The results are summarized in Table 3.3.



Figure 3.5: Fibres of a sample after burn-off.

Density values were set at 2.58 g cm^{-3} for e-glass, and 1.19 g cm^{-3} for the epoxy [12, 13]. The corrected value of V_f is calculated by omitting the layer of excess epoxy that accumulated on the exterior of the pipe, as this region of pure epoxy has been ignored in the model.

Table 3.3: Material weights and V_f found through burn-off. Corrected V_f omits the pure-epoxy region at the exterior of the pipe.

Measured data	Value
Epoxy weight	7.81 g
Fibre weight	12.98 g
V_f fibre	0.43
Corrected V_f fibre	0.48

3.3 Experimental setup

3.3.1 Damage creation

Segments of the GFRP-pipe were placed in a metal cradle and impacted by a 2.9 kg impactor guided by a rail that constricted all degrees of freedom except vertical movement. The impactor had a tip diameter of 16 mm, and the impact was centred on the top of the pipe. A schematic illustration of the set-up with dimensions is presented in Figure 3.6.

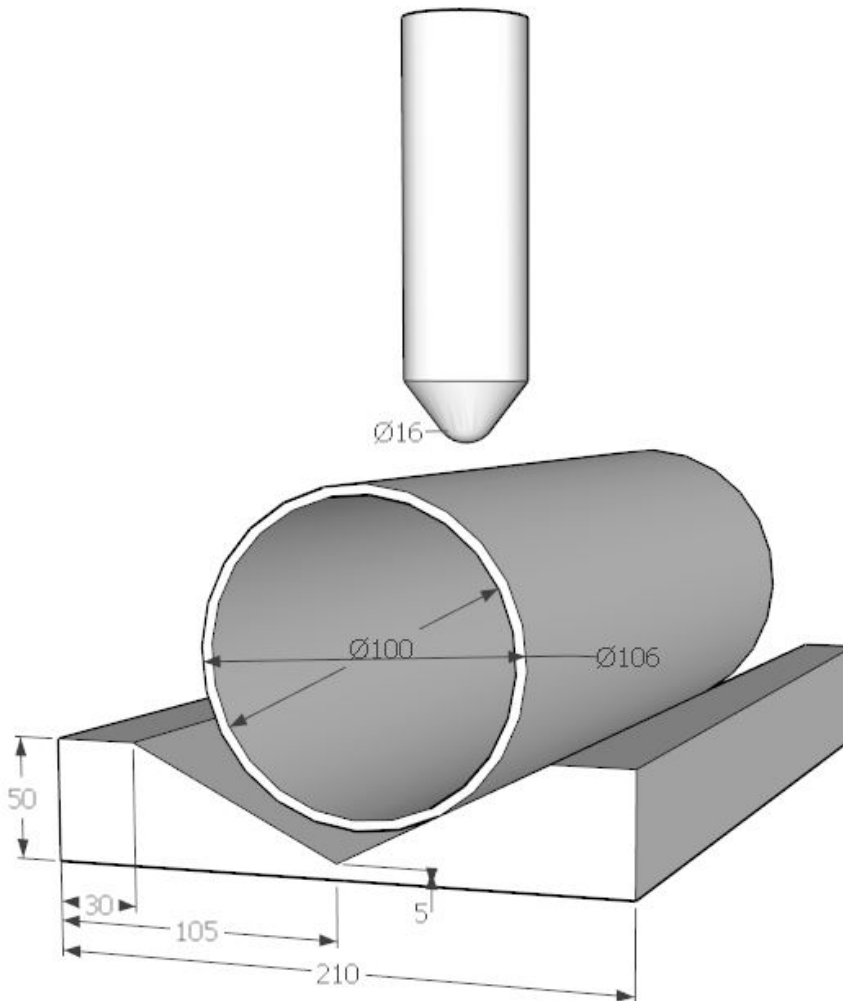


Figure 3.6: Pipe, impactor and cradle with dimensions.

The impactor was dropped on the samples from heights of 1.5 m (42.7 J) and 1.0 m (28.4 J). After impact the impactor was lifted before rebound impacts occurred. A total of three test specimens were impacted for both energies.

The resulting damage can be divided into three types:

- Delamination
- Fibre failure
- Matrix cracking

The delamination was detected by using a strong backlight. For matrix cracking, only the larger cracks present near the impact were seen by the naked eye. The fibre failure, which was restricted to compressive damage could be detected in good lighting. Through burn-off tests the fibre failure was proven to be total in the visible cracks (Figure 3.7). No fibre damage was present apart from in the visible cracks (Figure 3.8). Since these tests indicate that fibre failure can easily be seen, the state of the fibres was judged visually for the remaining specimens.



Figure 3.7: The left image shows a visible compressive crack of fibres at the location of impact, on the outside of the pipe. The right image shows that the fibres are broken in this area, and that the damage extends through the entire hoop layer. The red rectangle is a strain gauge used to measure strain during impact.

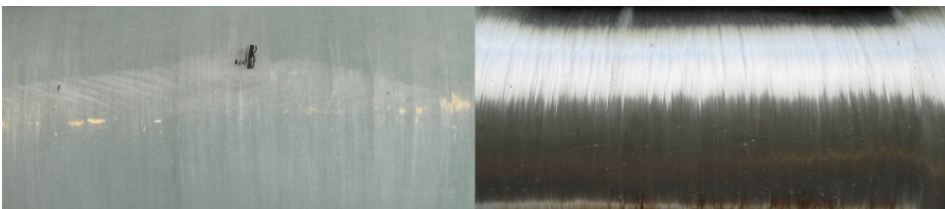


Figure 3.8: The left image shows an impact with no visible fibre failure. The right image confirms that no fibres are broken.

3.3.2 Evaluation of elastic response

The general stiffness response of the pipe was judged by impacting a specimen with a strain gauge attached. The strain gauge was glued to the inside of the pipe in the hoop direction, just below the point of impact (Figure 3.9). This gave information regarding the elastic behaviour of the pipe during impact, which again is directly related to the stiffness. Measurements were taken at 9600 kHz using a Spider-8 data acquisition device.



Figure 3.9: Pipe being impacted while strain is continuously measured.

Numerical method

The trade-off between accurately representing the scenario in question, and making simplifications to reduce computational time was a key factor when building the numerical model. Due to the complex nature of the problem, as few simplifications as possible were made, since it was difficult to predict which simplifications were benign, and which could severely alter the results.

In this model, the following simplifications were made:

- The distinct layers were modelled as continuum shells with different elastic and strength parameters in fibre direction and normal to the fibre direction.
- The model was divided into two regions. One finely meshed region in vicinity of the damage, and a coarse region far away from the damage.
- The delamination was modelled by implementing a 0.01 mm cohesive layer between the layers in the damage region. No delamination may occur elsewhere.

The interlaminar damage was modelled by the use of degradable cohesive elements, and the intralaminar damage by Hashin's failure criterion. The finely meshed area in the vicinity of the damage had dimensions of 150 mm in the longitudinal direction, and 120 mm in the circumferential direction. At these dimensions, the damage stayed within the bounds of the damage zone.

Impacts were simulated by subjecting the modelled pipe to an impact by a rigid element impactor corresponding to the experimental impactor.

An additional simplification is the modelling of materials as a continuum. The actual damage was made up of a discrete number of matrix cracks and buckled fibres. The model, on the other hand was continuous, where the damage state was represented by gradients. Therefore, the damage was smoother in the model than in the experiments.

4.1 Material parameters

4.1.1 Material stiffness parameters

Characterizing the material parameters of a filament wound pipe is somewhat demanding, as the geometry does not allow for easy fabrication of specimens suitable for testing. While using the filament winding technique to manufacture flat test specimens is an option, it is likely their material properties would differ from a pipe. The fibres are subjected to large forces towards the mandrel centre when winding pipes. This is an important aspect of the production which cannot be achieved when winding flat samples.

Flat plates produced by vacuum infusion are easier to test and produce, but as with a wound plate it does not equal the material of the pipe. However, some pragmatic sacrifices have to be made. Therefore, most of the material parameters in this thesis were based on material data for vacuum infused flat plates of HiPerTex W2020 fibres + Epikote MGS epoxy [14]. The pipe samples used in this thesis are made with the same epoxy, but a slightly different glass fibre (see table 3.1). Based on the result from the evaluation of elastic response (*Section 4.4*), no alterations of the stiffness parameters were made.

4.1.2 Delamination parameters

The delamination modelling requires parameters for stiffness, strength and fracture energies. Since delamination is simply debonding of fibres and subsequent breakage of the matrix, the transverse strength and shear strength of the vacuum infused plate provide a solid estimate for these values.

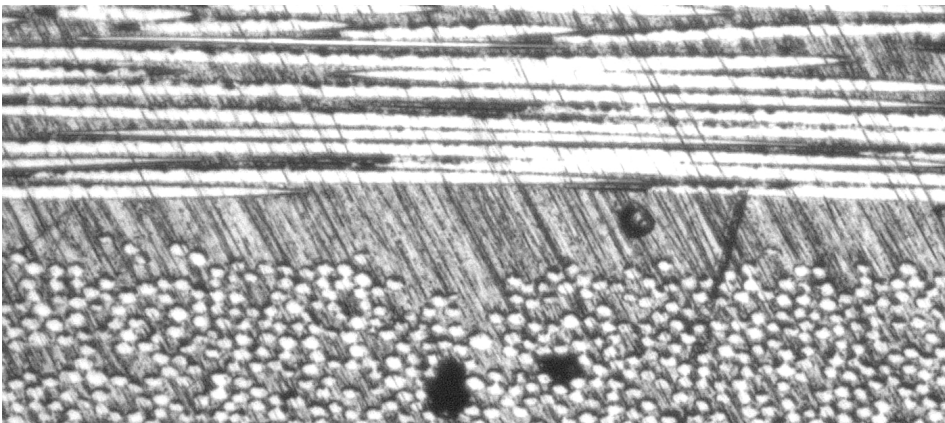


Figure 4.1: Microscopy image of pipe, showing the distinct matrix dominated region between layers. The top hoop layer is separated from the underlying layer by a region of pure epoxy.

For the stiffness value of the cohesive layer, the choice of value is less obvious. As shown

in Figure 4.1, there was a resin rich region between the layers. With this in mind it could be natural to give the cohesive layer stiffness according to the matrix stiffness alone. However, since the cohesive layers make up very little of the combined thickness of the pipe, this value is not of great importance. The cohesive stiffness was set equal to the stiffness of the matrix in transverse loading. This ensures that the response of the general and damage region is as uniform as possible. This was considered a good trade-off between having it very compliant, which would require very large deformations before damage stresses are reached, and having it too stiff, which reduces the stable time increment and therefore increase computational time. The stable time increment is calculated based on element size, stiffness and density.

Critical energy release rate data is needed to determine how the delamination evolves. The G_{IC} for a filament wound GFRP has been measured by Perillo et al. [15], and this value was therefore used. The values of G_{II}^C and G_{III}^C were not directly acquired, as measurements were not found for any wound GFRP-pipe. These values were assumed equal, and were roughly based on measured values for flat GFRP-plates [16]. Because of differences in production techniques, the energy release values from flat plates were modified to better reflect the experimental damage.

The damage evolution model used was the Benzeggagh-Kenane model with mixed mode behaviour power calculated by G. Perillo [14].

4.1.3 Hashin damage parameters

The damage onset parameters for the Hashin damage were set according to the flat plate measurements by Perillo et al. [14].

For the damage evolution, fracture energy both in tension and compression, for both the transverse and axial directions were needed (Figure 4.2). The transverse tensile fracture energy corresponds to the measured G_{IC} . Its compressive counterpart was assumed equal.

For the fracture energy in the axial direction, relevant measured values were unavailable, as fibre pull-out, micro-buckling stress etc. varies greatly with fibre diameter, fibre material, cohesion, fibre waviness etc. It is however known that this axial value is vastly greater than the transverse one, as it breaks the fibres, which have much larger strain energies than the matrix. The value is set at 150 N mm^{-1} for tensile fracture, and 75 N mm^{-1} for compressive fracture. This was assumed to be in the ballpark of actual values, but is not based on measured data. These values were chosen as they were found to best represent the experimental damage.

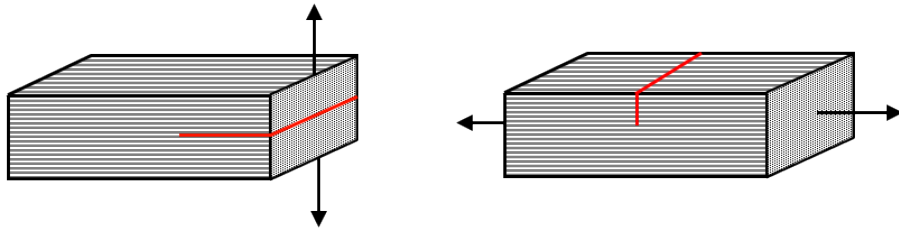


Figure 4.2: The left figure shows transverse fracture plane. The right figure shows the axial fracture plane. Fibre direction is indicated by the black lines.

Since the shear stiffness is governed largely by the state of the matrix, and the matrix is heavily damaged in the impact, steps were taken to avoid zero energy modes related to the destruction of shear stiffness for the elements.

The method used was adding viscosity parameters, causing the tangent stiffness matrix to be positive regardless of static stiffness. The value of the viscosity parameters were small compared to the characteristic time increment for the fibre direction, where damage is not extensive. For the matrix direction where damage is large, the viscosity parameters were also large to avoid zero energy modes. This improved the convergence rate in the softening regime, without compromising the results. It was also a necessity, as the shear damage quickly accumulates without it, causing the model to break down.

4.1.4 Material data table

All of the material parameters used in the model are presented in Table 4.1.

Table 4.1: Material parameters and their values for FE-model.

Property	Value
General composite parameters	
Elastic modulus ^a	$E_1=44.8$ GPa, $E_2=E_3=12.1$ GPa
Shear modulus ^a	$G_{12}=G_{13}=G_{23}=3.4$ GPa
Poisson's ratio ^a	$\nu_{12}=\nu_{13}=0.3$, $\nu_{23}=0.5$ ^b
Density ^a	1230 kg m ⁻³
Friction coefficient ^b	$\mu=0.3$
Hashin failure parameters	
Failure initiation stress ^{a+c+d}	$X_t=1006$ MPa, $X_c=487$ MPa, $Y_t=46$ MPa, $Y_c=132$ MPa, $S_{12}=S_{13}=S_{23}=42$ MPa
Longitudinal fracture energy ^{b+d}	$G_{tl}=150$ N mm ⁻¹ , $G_{cl}=75$ N mm ⁻¹
Transverse fracture energy ^{a+d}	$G_{tt}=0.83$ N mm ⁻¹ , $G_{ct}=0.83$ N mm ⁻¹
Viscosity coefficient ^b	1E-8 for fibre directions. 1E-1 for transverse directions
Cohesive parameters	
Elastic modulus of cohesive elements ^a	$E_{nn}=12.1$ GPa, $E_{ss} = E_{tt} = 3.4$ GPa
Density ^a	1230 kg m ⁻³
Failure initiation stress ^a	$t_n^c=46$ MPa, $t_s^c=t_t^c=49.5$ MPa
Critical strain energy release rate ^c	$G_{Ic}=0.83$ N mm ⁻¹ , $G_{IIc}=G_{IIIc}=1.80$ N mm ⁻¹ ^b
BK power ^a	$\eta = 1.4$

^aEstimated based on material data for HiperTex/Epoxy.

^bAssumed.

^cX and Y is in the fibre direction, and perpendicular to fibre direction respectively.

^dt and c represent tension and compression respectively

^eMeasured for similar GFRP-pipe[15]

4.2 Model buildup

The model featured the impactor and the pipe, which was divided into a damage region and a general region . The pipe was supported by a cradle during the impacts.

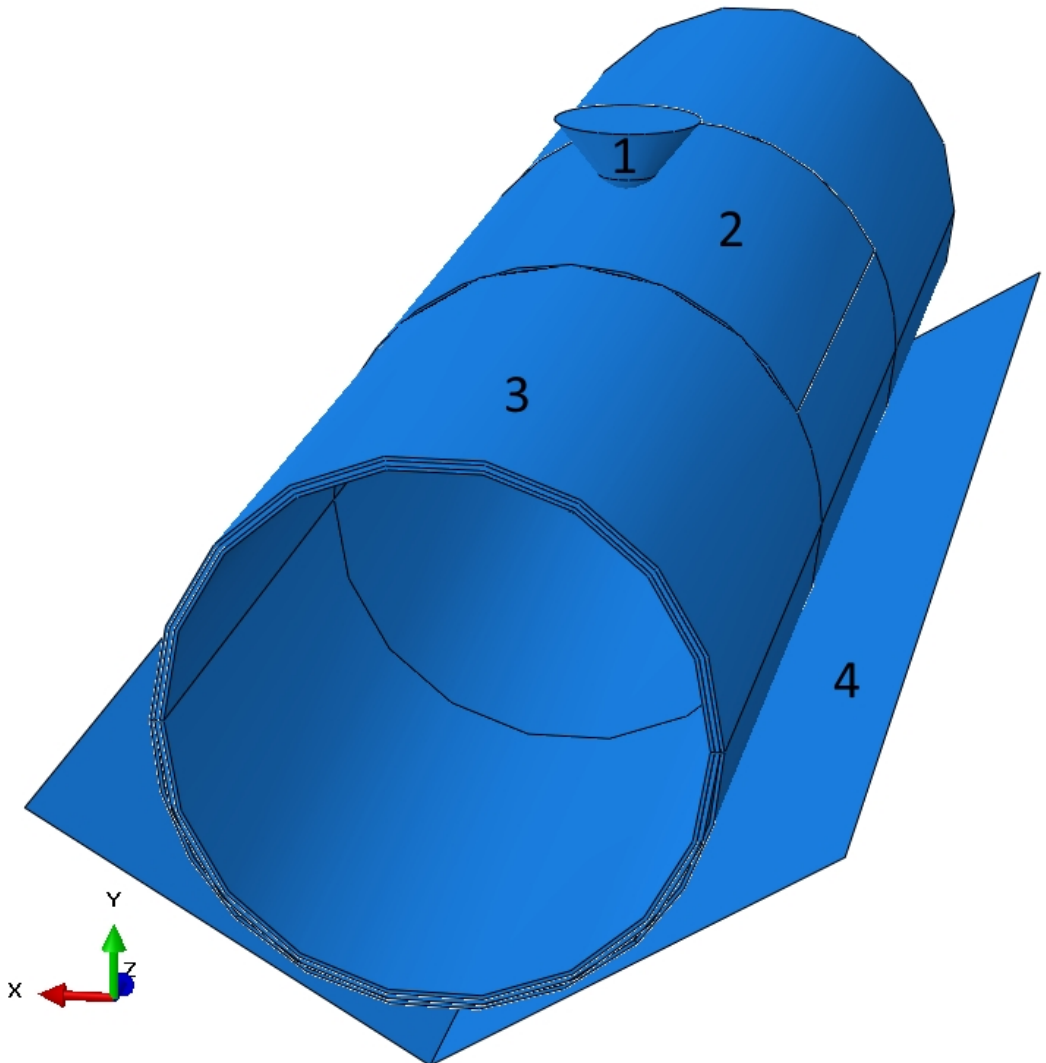


Figure 4.3: Overview of the FE-model. The impactor (1), damage region (2), general region (3) and cradle(4) are marked.

Impactor

The impactor was modelled as a rigid shell. It had a tip diameter of 16 mm, and a point mass of 2.9 kg at its reference point. Its movement was restricted to only the vertical direction. The impacts were simulated by giving the impactor an initial velocity corresponding to the impact velocity from the dropped height.

Contact between the impactor and the pipe was modelled using hard-contact and a friction coefficient (Table 4.1).

Damage region

To reduce computational time, the model was divided into a damage region, and a general region. In the damage region the mesh density was higher, and the pipe was modelled as three distinct continuum shells. One for the inner hoop layer, one for the central 15° - 15° layer, and one for the external hoop layer. The three distinct layers were connected through two thin sections of cohesive elements, as shown in Figure 4.4.

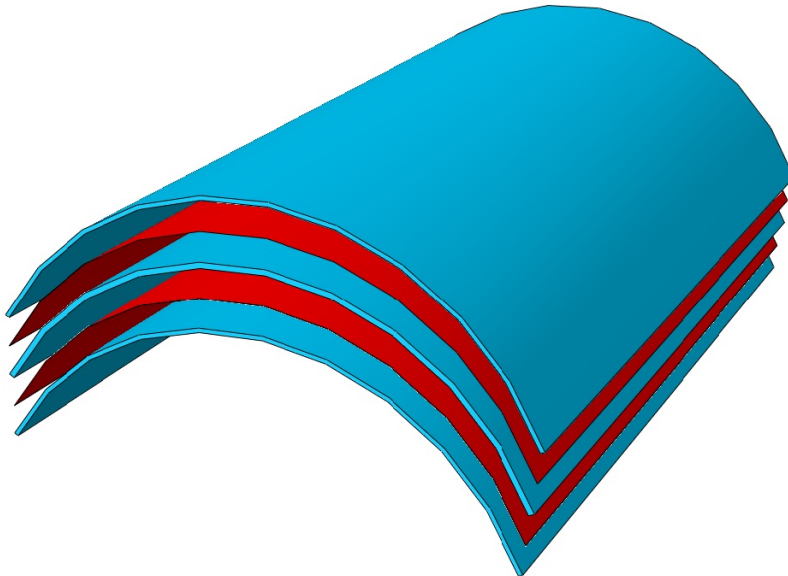


Figure 4.4: Exploded view of the damage zone. Blue instances are continuum shell regions and red instances are cohesive element regions.

The cohesive sections had a thickness of 0.01 mm. 0.005 mm of thickness was removed from the adjacent layers to accommodate the cohesive sections. The bottom nodes of the cohesive sections were tied to the continuum shell below, and the top nodes of the cohesive sections were tied to the continuum shell above. Both the cohesive and continuum

layers had similar mesh sizes, so that their nodes overlapped. This ensured that no initial penetration took place between elements.

In addition to the cohesive zone between layers, there were also contact conditions that came into play when the cohesive zone had degraded. The adjacent continuum shell surfaces were defined as contact pairs, with hard-contact and a friction coefficient (Table 4.1). This was needed to prevent penetration between layers, as the cohesive elements were deleted when their damage was total.

The continuum shell layers of the damage region were attached to the general pipe region by tying the edges of the damage layers to their respective general-region counterparts.

General pipe region

The region far away from the impact had a much more even stress field, and the damage was limited to very small degrees of matrix damage. Therefore the numerically costly cohesive layers and the higher mesh density is not needed. As with the damage region, the pipe was divided into its respective layers, the outer hoop layer, the central 15° - 15° layer and the inner hoop layer. These regions were tied together by tying the translations of their overlapping nodes together.

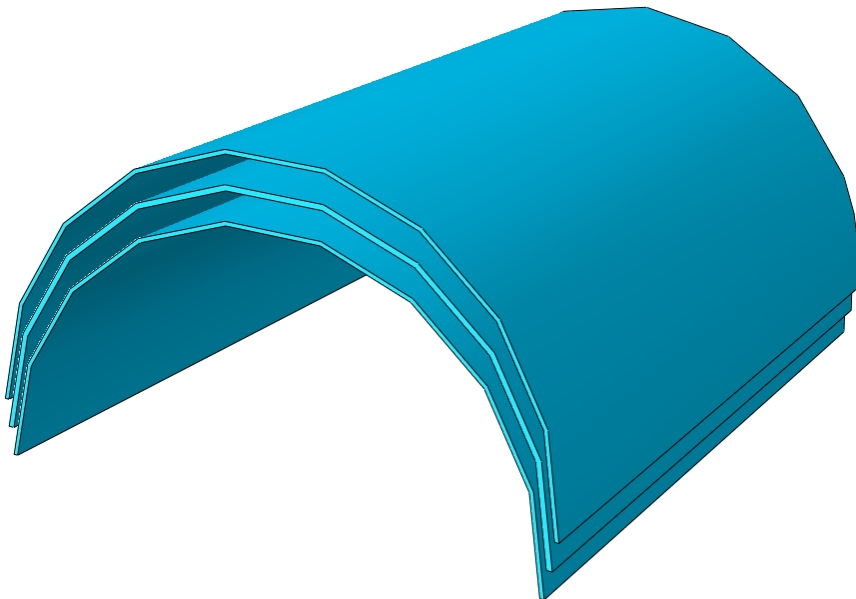


Figure 4.5: Exploded view of the general region. The general region was modelled as three distinct layers, connected by tie constraints.

Cradle

The cradle in which the pipe was seated during the experiment was modelled as a rigid shell. Between the cradle and the pipe, hard-contact with a friction coefficient was defined (Table 4.1). All movement of the cradle was constrained.

An overview of the model properties can be found in Table 4.2.

Table 4.2: Overview of model properties for all parts of the assembly.

Property	Value
Impactor (1)	
Element type	Discrete rigid element (R3D4)
Boundary conditions	$U_x = U_z = 0$ $U_{rx} = U_{ry} = U_{rz} = 0$
Velocity in Y direction	Variable
Tip diameter	16 mm
Mass	2.9 kg
Gravity load	28.45 N
Damage zone (2)	
Element type	Continuum shell (SC8R) Cohesive element (COH3D8)
Boundary conditions	Shells tied to cohesive zone Shells tied to general pipe region
Contact interaction	Contact between adjacent shells and impactor Normal behaviour: Hard-contact Tangential behaviour: Penalty, $\mu = 0.3$
General region (3)	
Element type	Continuum shell (SC8R)
Boundary conditions	Adjacent shells tied together Contact between exterior shell and cradle
Contact interaction	Normal behaviour: Hard-contact Tangential behaviour: Penalty, $\mu = 0.3$
Cradle (4)	
Element type	Discrete rigid element (R3D4)
Boundary conditions	$U_x = U_y = U_z = 0$ $U_{rx} = U_{ry} = U_{rz} = 0$

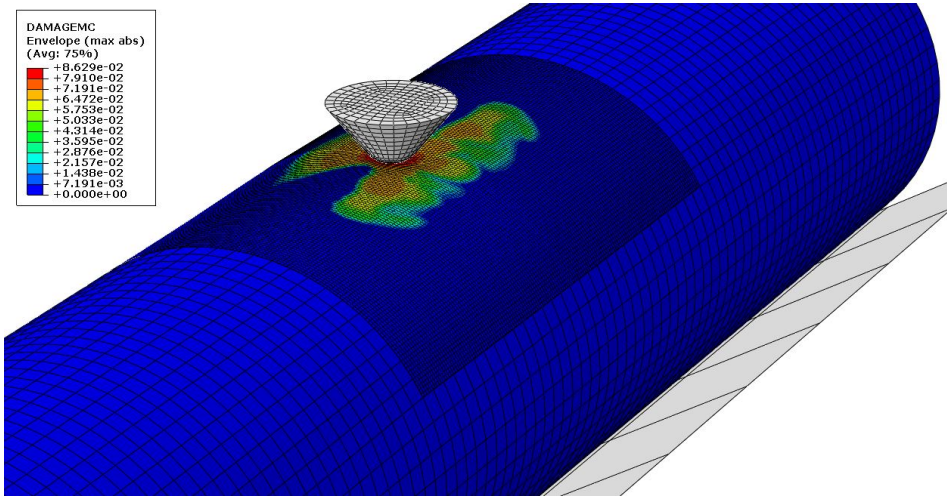


Figure 4.6: Model during impact. Displayed value is matrix damage envelope due to compression.

4.3 Mesh convergence analysis

Analyses were run with elements of varying in plane dimensions to determine if the mesh density was adequate. For the general-region part of the model, a simple pipe with element sizes of 20×20 , 10×10 and 5×5 mm was subjected to an impact of 42.67 J and the deflection over time was compared between meshes. As seen in Figure 4.7, the medium and fine mesh were close to the convergence limit. The peak displacement only increased by 3 % from the medium to the fine mesh. The fine mesh (5×5 mm) was therefore deemed to be adequate for the general region (Figure 4.3).

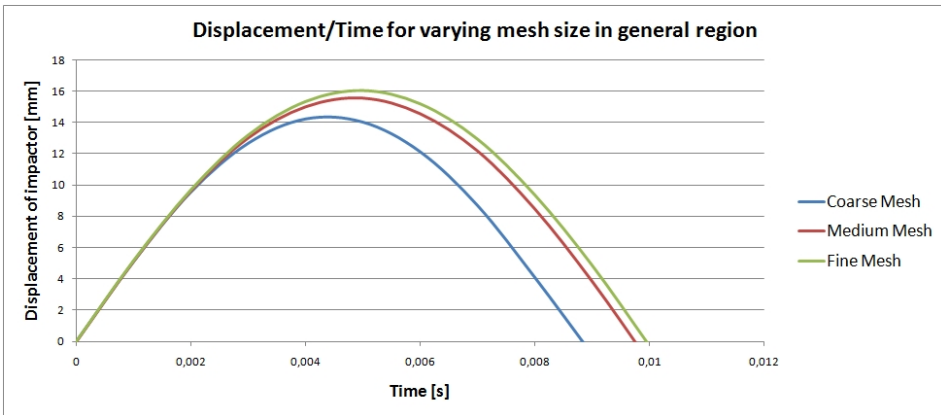


Figure 4.7: Convergence with refinement of general region mesh. The displacement over time for the impactor approached the convergence limit. Only a 3 % difference in peak displacement between medium and fine mesh.

For the damage-region of the model, the mesh size is more crucial as it influences both the Hashin damage, delamination and the contact interaction between the impactor and pipe. Elements with in-plane dimensions of 4×4 , 2×2 , and 1×1 mm were analysed. Analyses were made for a model featuring delamination, and one without it. As seen in Figure 4.8, the elastic response of the pipe has converged almost completely for the model when damage is not included. This indicates that the properties concerning the interaction between the impactor and the pipe are well represented, even by the coarse mesh. It does not however say anything about how well the mesh performs with regards to Hashin damage and delamination.

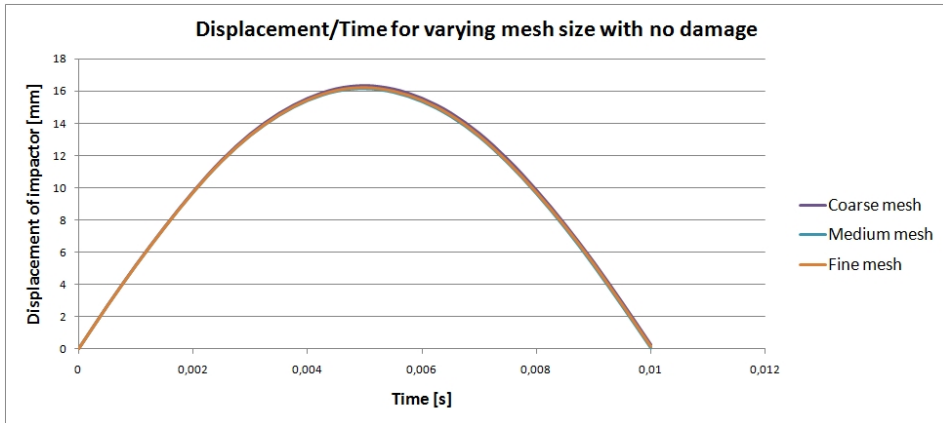


Figure 4.8: Convergence with refinement of damage region mesh in a model with no Hashin damage or delamination. The three meshes produce near identical displacement curves.

The coarse mesh seems adequate for the continuum shell layers when judging from Figure 4.8. However, as shown in Figure 4.9, the element size influences the shape and extent of the concentrated fibre damage. Although the mesh density does not affect the general stiffness response for an impact with low values of damage, it is important during damage propagation when the damage is severe. The size of this mesh is also tied to the size of the cohesive mesh, since the curvature will be approximated differently when using more elements. It must therefore be refined to match the required mesh for the cohesive layers.

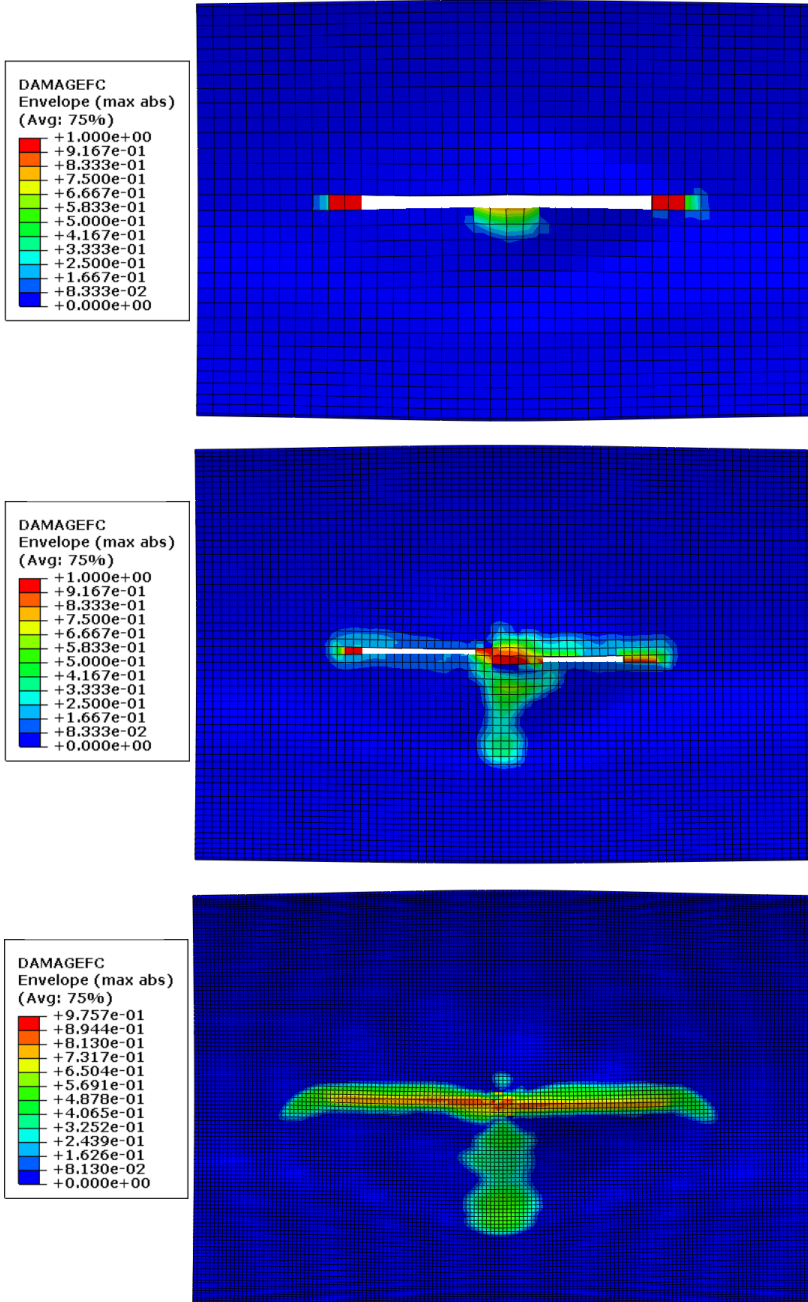


Figure 4.9: Compressive fibre damage in top layer for the coarse, medium and fine mesh. Model features both delamination and Hashin damage. White elements have no stiffness and are removed. The shape and extent of damage is greatly influenced by the mesh size. Both magnitude and shape of damage is affected by the mesh size.

Based on Figure 4.9, the fine mesh was judged to be necessary when modelling Hashin damage. If computational time had been lower, an ever finer mesh would have been a possibility (Table 4.3).

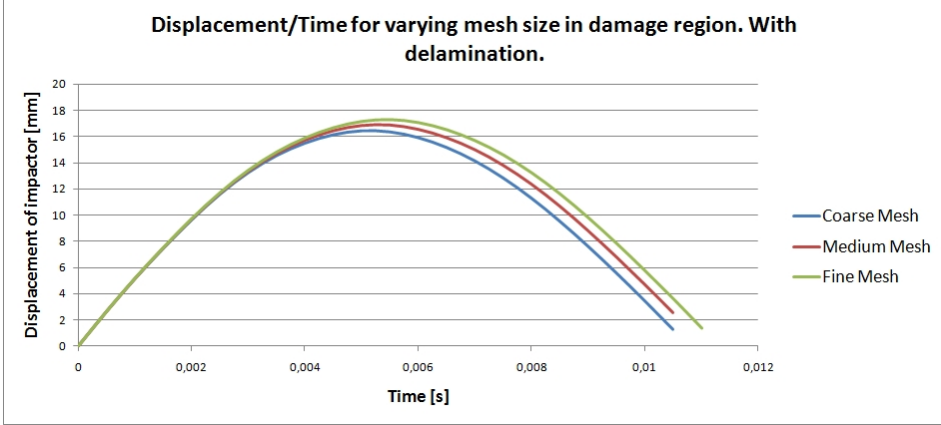


Figure 4.10: Convergence with refinement of cohesive layer mesh. Increasing mesh density affected the stiffness of the pipe.

As seen in Figure 4.10, refining the mesh of the cohesive layers resulted in changes for the displacement curve. The stiffness variation can be attributed to the changes in the area and shape of the delamination-zone. In fact, the general shape changes abruptly between the 4×4 and 2×2 mm mesh, as shown in Figure 4.11. This is in agreement with Equations 2.16 and 2.17, which recommend element sizes of $\approx 1 \times 1$ mm.

The percent-wise difference in maximum deflection is 2.8 % for coarse to medium mesh, and 2.2 % for medium to fine mesh. Combined with the state of delamination shown in Figure 4.11, it was concluded that both the medium and fine mesh have converged adequately with regards to delamination.

The stable time increment is heavily dependent on the characteristic length of the smallest element in the model. Due to this the computational time of the model is heavily influenced by the mesh density in the damage region. The CPU-time, stable time increment and number of elements for each mesh is shown in Table 4.3.

Table 4.3: Effect of mesh size in damage region on calculation time. 2 cores of i5 2.6 GHz were used. Number of elements is total number of elements for the entire model.

Element size in plane [mm]	Number of elements	Stable time increment [s]	CPU-time [s]
4x4	20487	1.02E-07	4235
2x2	36951	9.36E-08	9742.4
1x1	104183	7.18E-08	22183

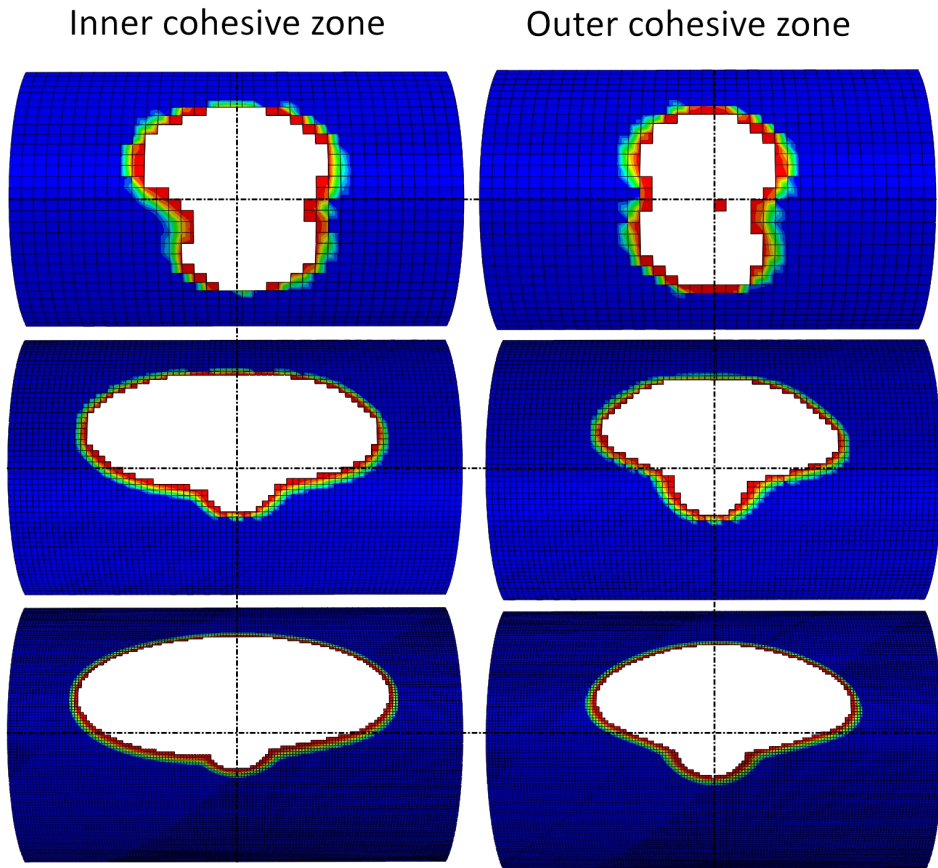


Figure 4.11: Increasing mesh density affects the size and shape of the delamination. Coarse, medium and fine mesh shown. Convergence in both shape and size is good at element sizes below 2×2 mm. The colour of the elements represent the state of stiffness degradation. Blue elements are undamaged and red elements have high levels of damage. White region consists of deleted elements with no stiffness.

4.4 Model stiffness evaluation

The initial material parameters used in this thesis were based on HiPerTex R-Glass, whereas the actual experiments were conducted on a slightly more compliant E-glass (10% difference in modulus of elasticity). There was also a difference in fibre fraction between the wound pipe and the vacuum infused specimens. However, since there were many uncertainties in the transition from a vacuum infused flat plate to a filament wound pipe, adjustments have not been made based on the difference in fibre stiffness and volume fraction alone. Instead the validity of the stiffness data was evaluated based on the impact time of an experimental impact, compared with the impact time of a numerical impact.

To determine the duration and strain during an impact, a pipe was fitted with a strain gauge and impacted. The strain gauge was placed directly under the point of impact, inside the pipe.

As shown in Figure 4.12, the experimental and numerical impact times are in good agreement before any adjustments. Therefore, no adjustments were made to any of the stiffness parameters, as they were found to adequately reflect the experimental stiffness.

The difference in strain magnitudes were due to numerical strain being the maximum value directly below impact, whereas the measured strain was an averaged strain over a 5 mm strain gauge. Therefore the magnitudes cannot be directly compared, but both curves reflect the state of the impact.

The drop in strain at 1 ms for both curves corresponds well with the initiation of delamination (Figure 5.6).

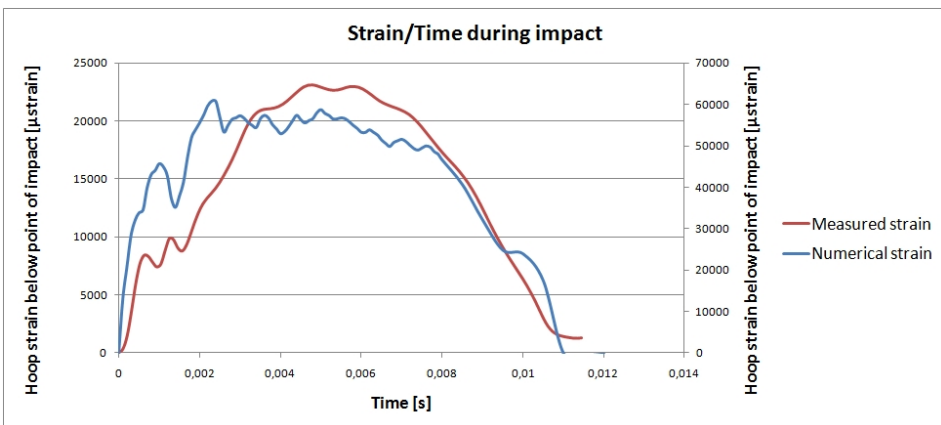


Figure 4.12: Correlation between experimental and numerical strain during impact. Sampled in hoop direction at the inside of the pipe, directly below impactor. Left axis for measured strain, right axis for numerical strain. Numerical strain sampled at element directly below impactor, measured strain sampled by a strain gauge below impactor.

4.5 Choosing damage predictors

4.5.1 Delamination damage

Deleted elements were chosen to represent visible delamination. Each element possesses four integration points, and the state of damage is on the scale from 0 to 1 for each point (also referred to as a percentage of total damage later in the text). When damage reaches 1 for all integration points, zero stiffness remains and the element is deleted. Using deleted elements to represent visible delamination is arbitrary. Any combination of damage values > 0 in the different integration points could have served. The border between damaged and deleted elements is very thin (Figure 4.13). Therefore the choice of damage prediction parameter won't have a great influence.

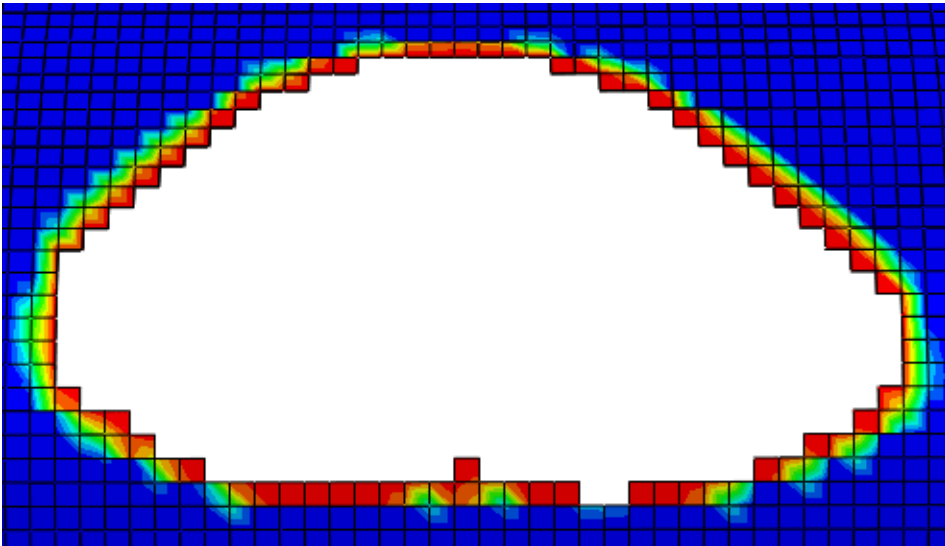


Figure 4.13: Border between damaged and undamaged cohesive elements with smoothing. Only one or two elements separates the undamaged elements from the deleted elements. The colour of the elements represent the state of stiffness degradation. Blue elements are undamaged and red elements have high levels of damage. White region consists of deleted elements with no stiffness.

4.5.2 Intralaminar damage

The choice of parameters that mirror fibre- and matrix-damage is more complicated. Each layer has three integration points through the thickness, and each of these points contain state variables for the damage of fibre and matrix. For the cohesive elements, the damage variables of integrations points are closely connected. This is not the case for the section points of the continuum shell, where the state of damage is very different between section points within the same element.

Choosing deleted elements as the fibre damage predictor will be non-conservative, as the nature of shell elements makes the damage travel slowly through the section points of a layer. The elements will not be deleted until no stiffness remains in any of the section points. In reality the fibres break throughout the thin layer abruptly after the top fibres buckle. In the model the lower section points break down a lot slower than the top ones. For this reason a crack was assumed to be created through the ply when any of the section points in the layer have their damage variable higher than 0.5.

The matrix damage extends far due to the low strength of the matrix. Due to the continuity of the model, the matrix damage is near constant over large areas. The actual scenario on the other hand, is a finite number of matrix cracks separated by regions of undamaged matrix. Predictions of the model are not made on the specific locations of any cracks, but rather an area in which matrix cracks are thought to be present. The high level of viscous damping employed to prevent zero energy modes keeps matrix damage levels low. Large values for the matrix damage variable is therefore not reached in the impacts. The predictor for matrix damage is therefore set to be any value of $d_m > 0$.

5.1 Experimental impact damage

For both the 1.5 m (42.67 J) and 1.0 m (28.45 J) impact the damage produced was mainly delamination, in addition to matrix cracks in the hoop direction for the inner and outer layer. The delamination was heavily one-sided for all impacts. Delaminations started at the apex of the pipe, and travelled downwards along the hoop direction.

Matrix damage occurred near the point of impact in the hoop direction for every sample, both internally and externally. Matrix cracks were numerous in the internal and external hoop layer, near the point of impact. For one of the 1.0 m impacts, and one of the 1.5 m impacts, compressive fibre failure created cracks near the impactor, through the top layer.

The average sizes of the delaminations are presented in Table 5.1. Images of the damaged regions are shown in Figures 5.1 and 5.2.

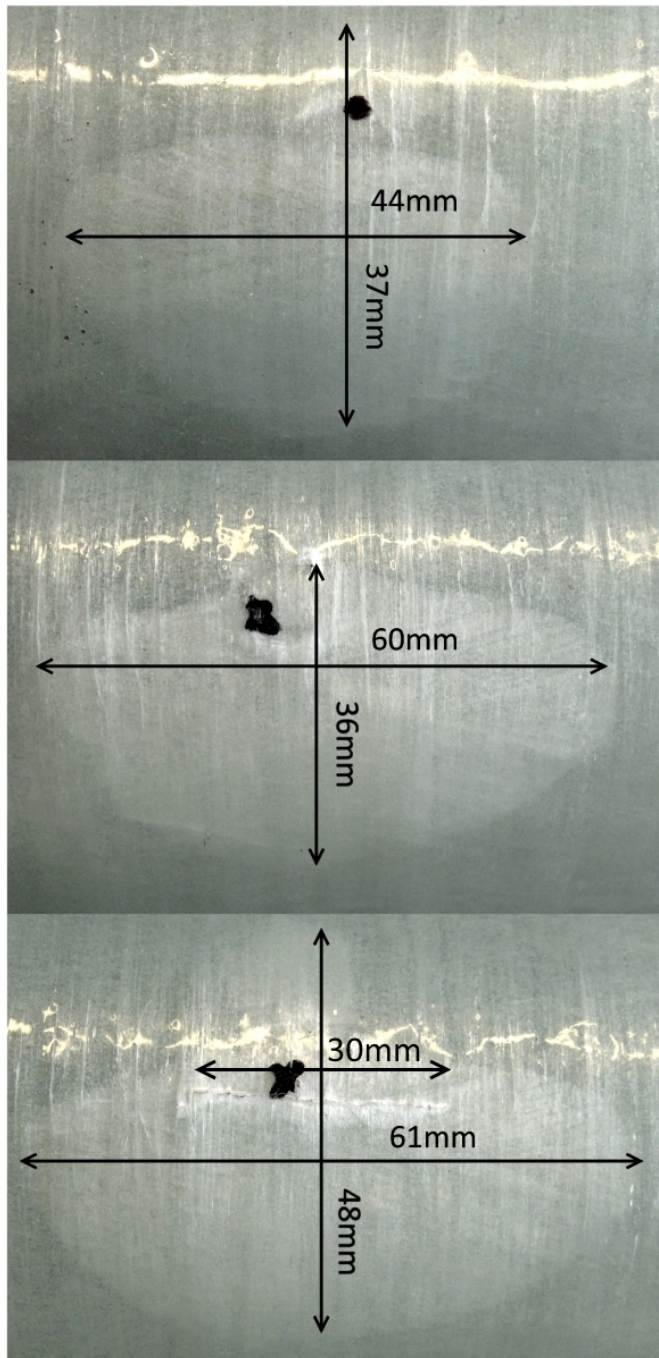


Figure 5.1: Damage from three identical 1.0 m (28.45 J) impacts. Matrix cracking and delamination clearly visible. Note the 30 mm fibre crack in the bottom sample. Burn-off tests confirmed that the crack goes through the entire top layer. Black dot/cross marks the point of impact.

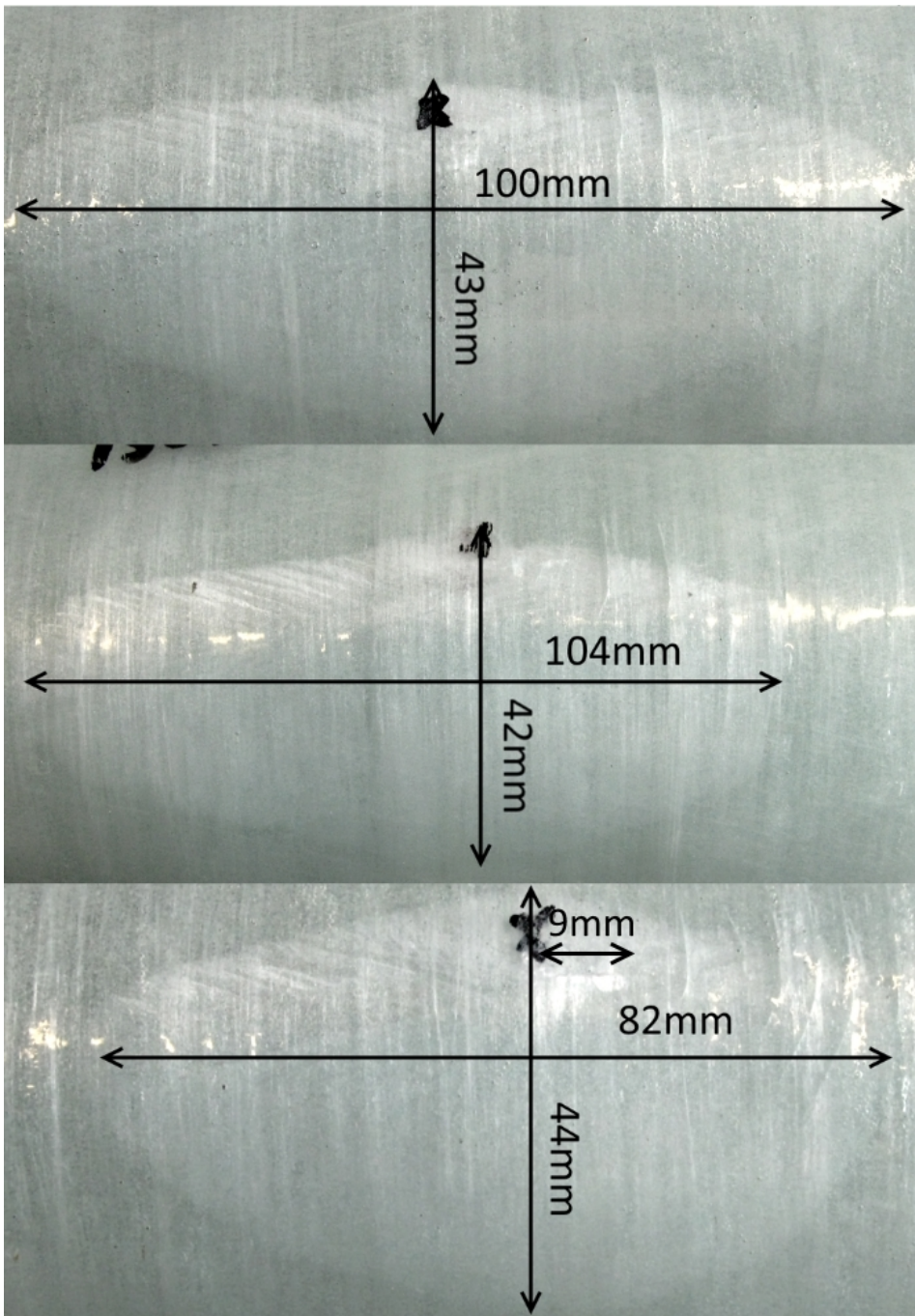


Figure 5.2: Damage from three identical 1.5 m (42.67 J) impacts. Matrix cracking and delamination clearly visible. Note the 9 mm fibre crack in the bottom sample. Burn-off tests confirmed that the crack goes through the entire top layer. Black dot/cross marks the point of impact.

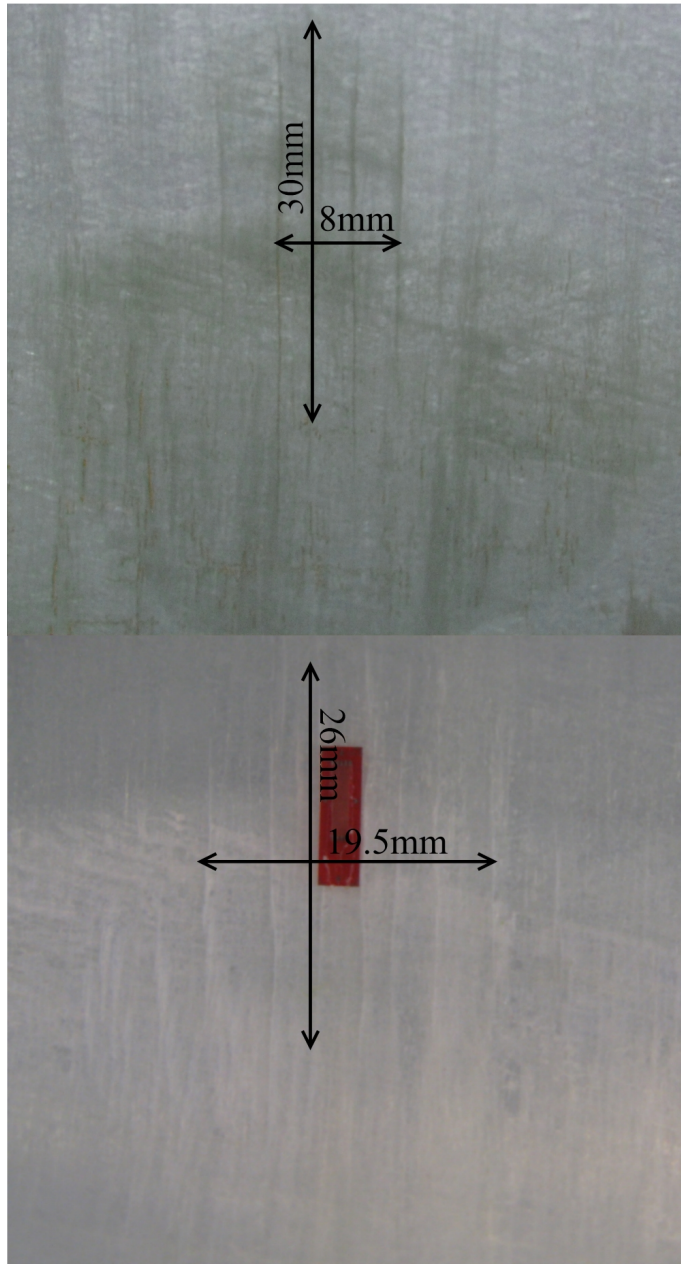


Figure 5.3: Internal matrix damage from 1m and 1.5m impacts (top and bottom). Large visible matrix cracks surround the impact location. Red square in bottom image is a strain gauge. Similar damage was present in all specimens. Arrows indicate area with large visible matrix cracks.

Table 5.1: Average size of experimental delaminations.

Drop height [m]	Longitudinal length [mm]	Hoop length [mm]
1.0	55	40.3
1.5	95.3	43

5.2 Numerical damage

5.2.1 Interlayer damage

With delamination parameters set according to Table 4.1, the delamination produced for the 1.0 m and 1.5 m impacts can be seen in Figures 5.4 and 5.5. The asymmetry from the experiments was reproduced with good accuracy in both shape and size.

The delaminations were produced in a model with no Hashin damage, since the majority of the test specimens did not present any fibre damage.

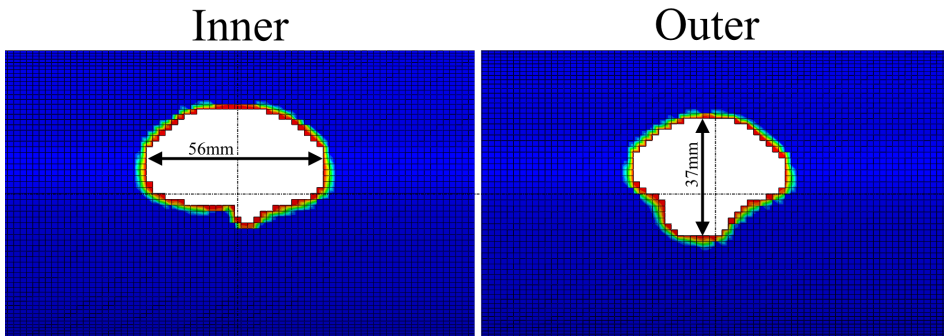


Figure 5.4: Numerical delamination from 1.0 m impact. The colour of the elements represent the state of stiffness degradation. Blue elements are undamaged and red elements have high levels of damage. White region consists of deleted elements with no stiffness.

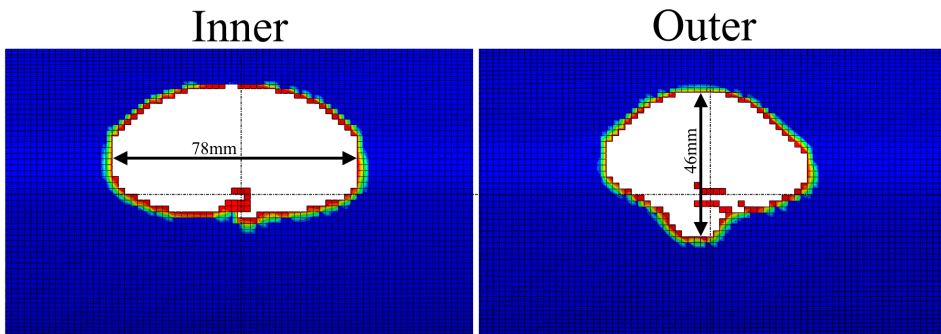


Figure 5.5: Numerical delamination from 1.5 m impact. The colour of the elements represent the state of stiffness degradation. Blue elements are undamaged and red elements have high levels of damage. White region consists of deleted elements with no stiffness.

The longitudinal and hoop length of the damage can be seen in Table 5.2.

Table 5.2: Size of numerical delaminations for both impact heights.

Drop Height [m]	Longitudinal length [mm]	Hoop length [mm]
1.0	56	37
1.5	78	46

5.2.2 Delamination evolution

Figure 5.6 illustrates the delamination propagation in the outer cohesive zone for the 1.5 m impact. The first delamination appears after 1.1 ms. It slowly evolves in a symmetric manner until 2.4 ms, where the asymmetry appears. After 2.5 ms it propagates almost exclusively in one direction. At 5.3 ms, the impactor is at its lowest point. The resulting damage is heavily one-sided. At 11 ms the impactor is no longer in contact with the pipe, and the pipe has returned to its origin. When returning to the original position, additional delamination consist mainly of heavily damaged elements that reach the threshold for deletion.

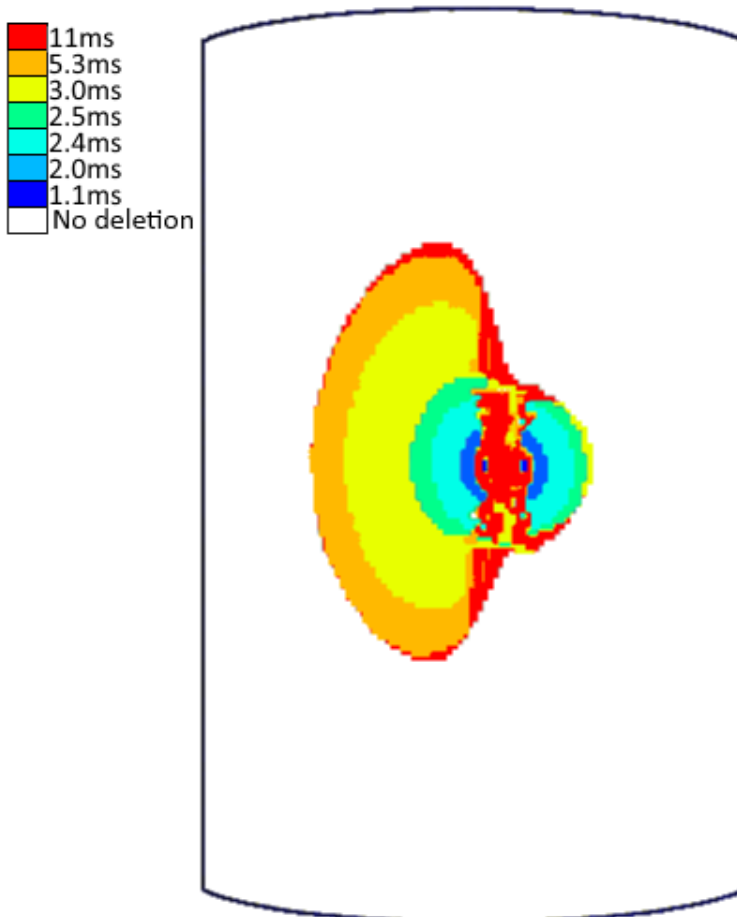


Figure 5.6: Evolution of deleted elements in outer cohesive zone for 1.5 m impact. Coloured regions represent extent of deleted elements at different times after impact. Maximum deflection at 5.3 ms.

To better relate the delamination evolution to the deformation of the pipe, the central arch of elements can be seen during impact in Figures 5.8 and 5.9. These figures show the row of elements directly below the impactor during the impact. Below the time-scale are the shell layers and cohesive layers, these illustrate the deflections and separations of the different layers. Above the two cohesive sections are viewed at the same point in time. This illustrates the state of element deletion in relation to the deformations of the pipe layers. Figure 5.7 shows these elements along with the rest of the model.

The output times are chosen to concisely sum up the evolution. At 1.1 ms the first elements are deleted. The growth is then symmetrical until 2.4 ms, where it become highly asymmetrical. At 5.3 ms the impactor reaches zero velocity, and at 11 ms the impactor bounces off the pipe surface.

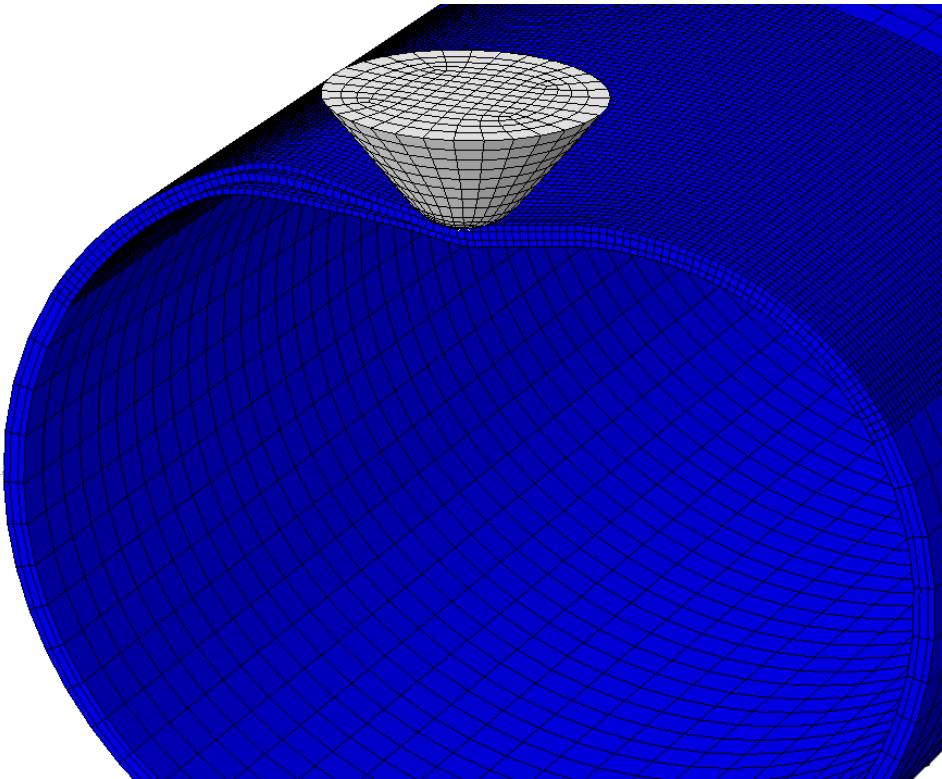


Figure 5.7: View cut of central element arch during impact. This row of elements is shown with progressing time in Figures 5.8 and 5.9.



Figure 5.8: Internal view of delamination as damage progresses. Bottom row shows separation of layers, top row shows which cohesive elements have been deleted. The same elements are displayed as time increases.

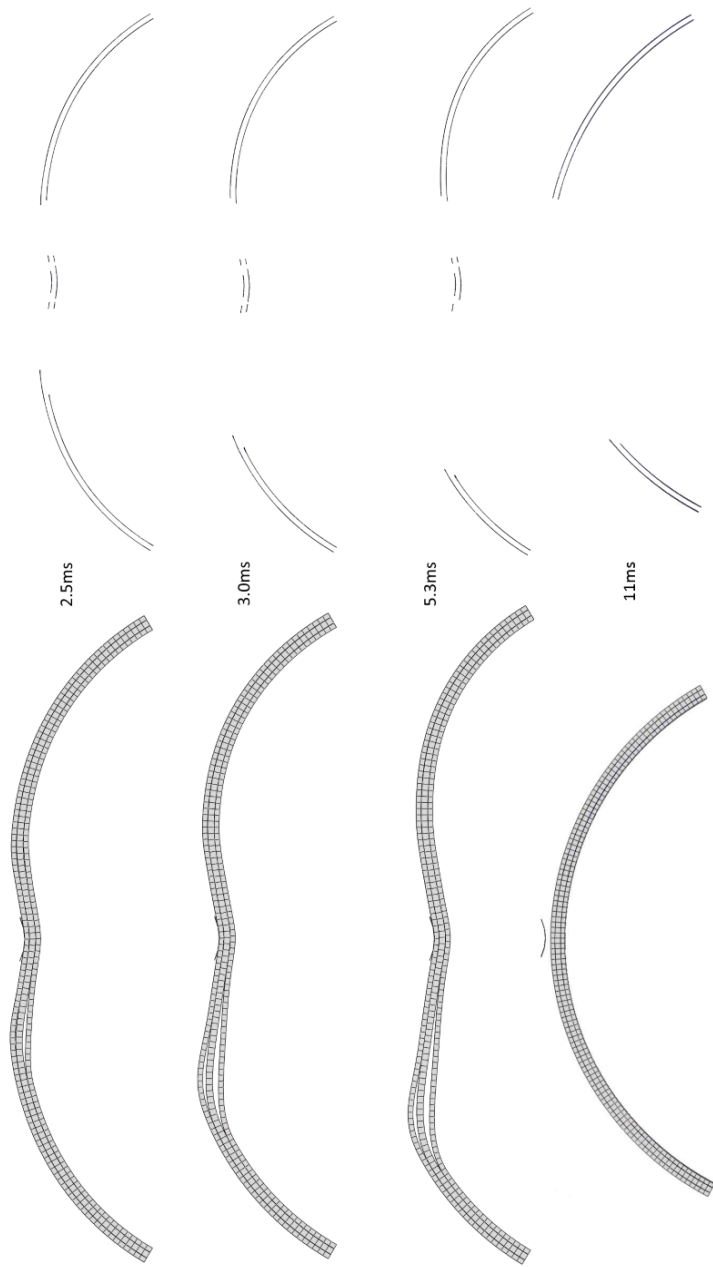


Figure 5.9: Continuation of Figure 5.8. Internal view of delamination as damage progresses. Bottom row shows separation of layers, top row shows which cohesive elements have been deleted. The same elements are displayed as time increases.

Stress during delamination

Figures 5.10 and 5.11 show the stress in the vicinity of the delamination at three points in time. As seen in Figure 5.10, the stresses are limited to shear for the first part of the delamination. When the delamination grows, there is also a wave of normal stresses created by the peeling of the adjacent plies (Figure 5.9). The distance between the edge of deleted elements and the peak stresses is due to heavily damaged elements with low stiffness in between. These figures show that the delamination is caused by shear to begin with, but changes to mixed-mode as the delamination progresses. See also *Section 5.2.4*, where the model sensitivity is investigated.

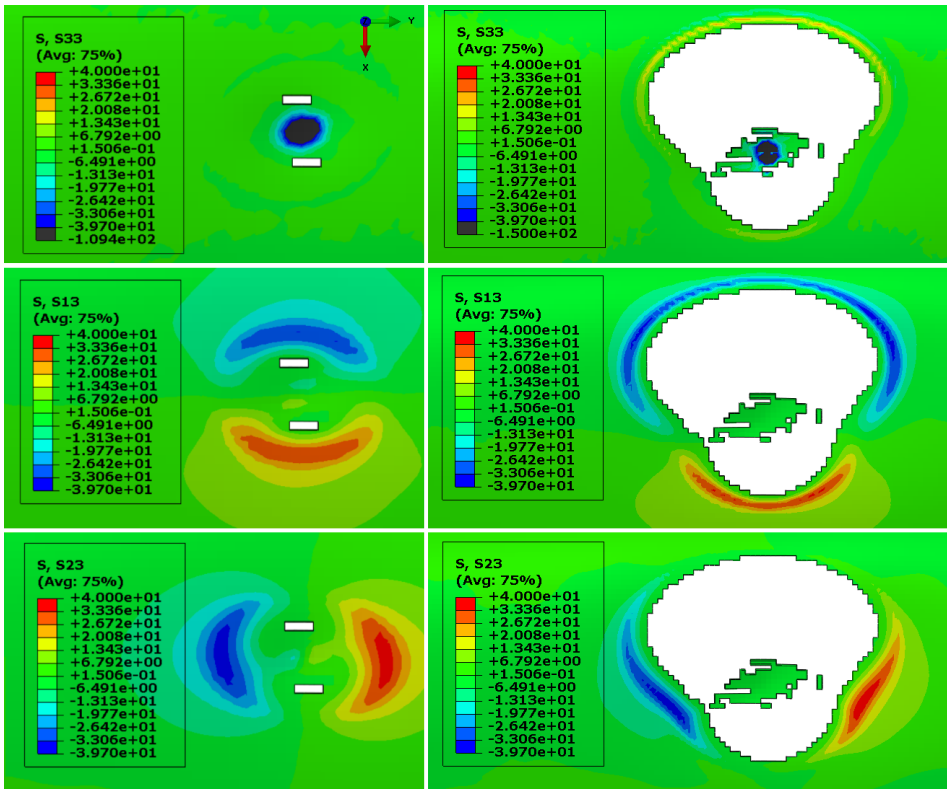


Figure 5.10: Stress distribution in inner cohesive layer. Left side, $t=1.1$ ms. Right side, $t=2.6$ ms. S33 is normal stress, S13 is shear in the XZ plane and S23 is shear in the YZ direction. Units are MPa.

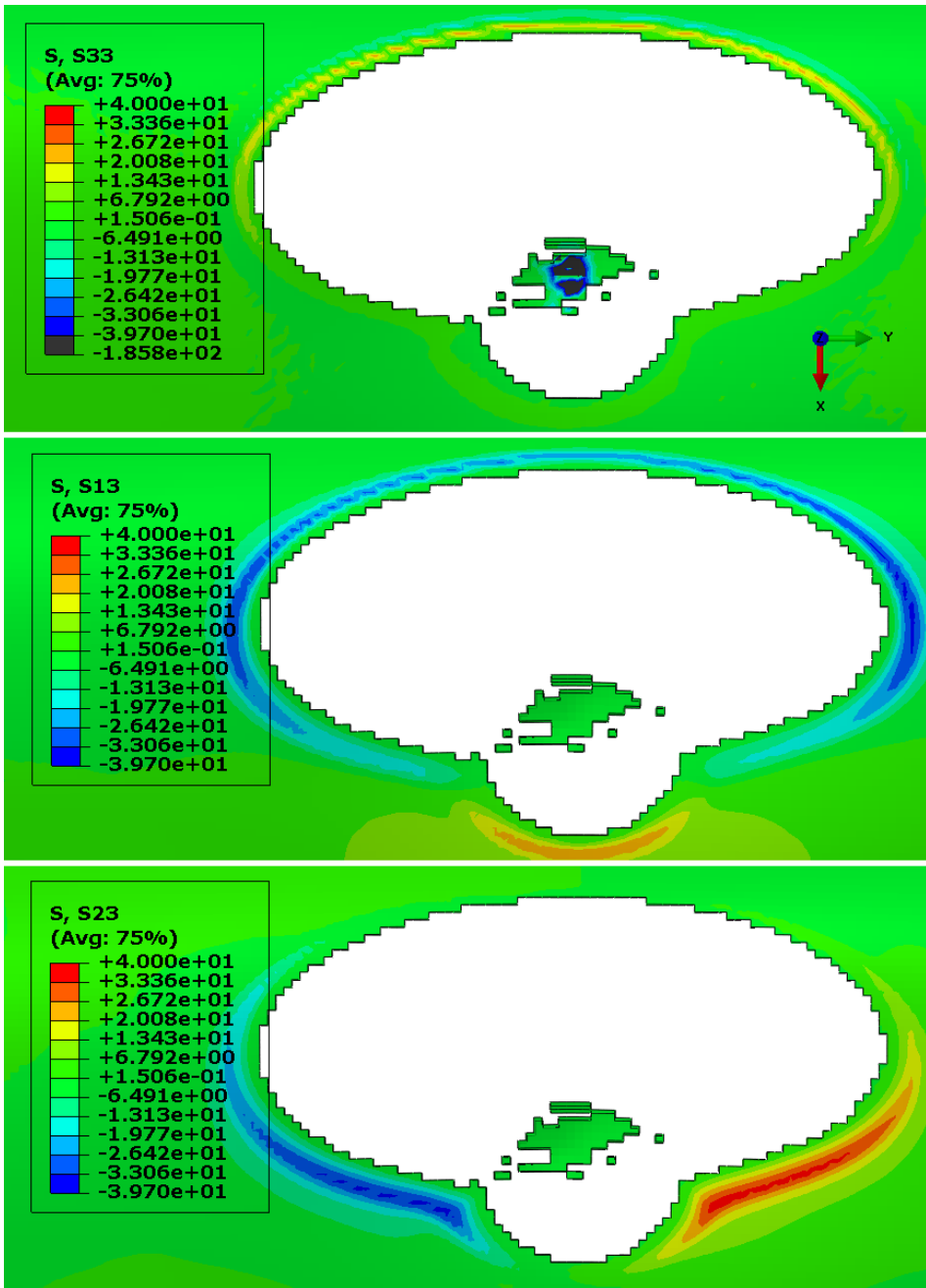


Figure 5.11: Stress distribution in inner cohesive layer. $t=3$ ms. S33 is normal stress, S13 is shear in the XZ plane and S23 is shear in the YZ direction. Units are MPa.

5.2.3 Effect on Hashin damage on delamination

The weakening of the fibres and matrix during impact affects the distribution of stresses between the layers, and therefore the delamination. Figures 5.12 and 5.13 shows the delamination from two 1.5 m impacts. Figure 5.12 has no intralaminar damage, and Figure 5.13 has identical cohesive parameters, as well as Hashin damage parameters according to Table 4.1. Only a minor difference can be seen between the delaminations in the model featuring Hashin damage and the one without it.

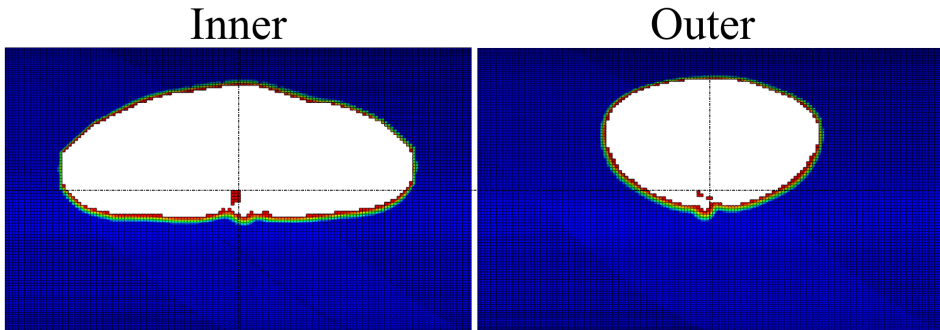


Figure 5.12: Delamination in inner and outer cohesive layer with no Hashin damage. 1.5 m impact. The colour of the elements represent the state of stiffness degradation. Blue elements are undamaged and red elements have high levels of damage. White region consists of deleted elements with no stiffness.

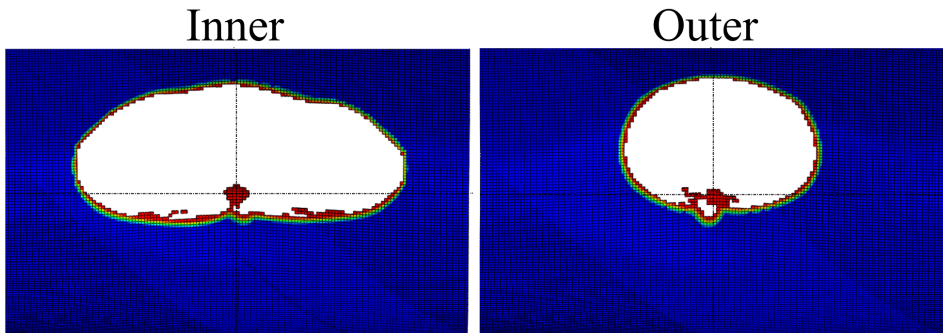


Figure 5.13: Delamination in inner and outer cohesive layer with Hashin damage. 1.5 m impact. The colour of the elements represent the state of stiffness degradation. Blue elements are undamaged and red elements have high levels of damage. White region consists of deleted elements with no stiffness.

5.2.4 Delamination sensitivity analysis

The cohesive elements are more sensitive to some parameters than others. A sensitivity analysis was performed on a 1.5 m impact to shed some light on the significance of various parameters. Each parameter that was considered important for delamination was increased and decreased by 50% relative to the base model (Table 4.1). The resulting differences were examined.

Since the effect of Hashin damage on delamination was shown to be minimal and the medium mesh was found to suffice for delamination, the following results are obtained from a model with no Hashin damage, using a medium mesh.

Below, the delaminations in the inner and outer cohesive layers are presented for a variety of different cohesive parameters. Figure 5.14 shows the delamination using the parameters from Table 4.3. These parameters were judged to best replicate the experimental data. Figures 5.15 to 5.18 show the delaminations when one set of parameters are reduced by 50%, or increased by 50%.

For G_{IC} and G_{IIC}/G_{IIIC} the low and high value corresponds to changing G_{IC} and G_{IIC}/G_{IIIC} from the base of 0.83 N mm^{-1} and 1.80 N mm^{-1}

For the low and high strength values the tensile and shear failure stresses of the cohesive layer were changed from the base of $t_n^c=46 \text{ MPa}$ and $t_s^c=t_t^c=49.5 \text{ MPa}$.

Similarly, for the low and high stiffness, the base values of $E_{nn}=12.1 \text{ GPa}$ and $E_{ss}=E_{tt}=3.4 \text{ GPa}$ were modified.

Finally two simulations were made where the point of impact was moved 2 mm and 4 mm to different sides of the apex.

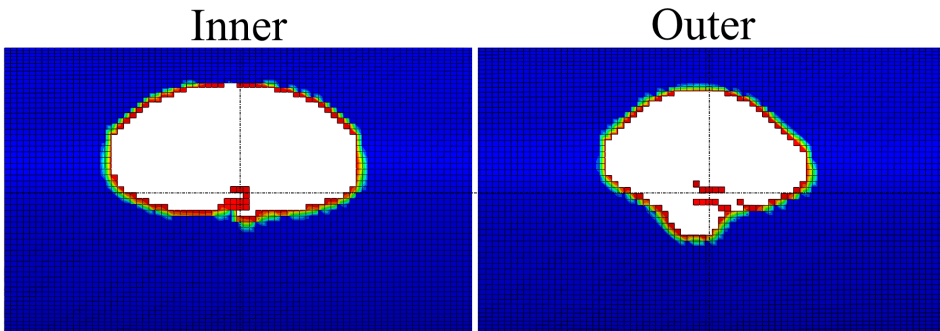


Figure 5.14: Delamination in inner and outer cohesive layer for the base model. The colour of the elements represent the state of stiffness degradation. Blue elements are undamaged and red elements have high levels of damage. White region consists of deleted elements with no stiffness.

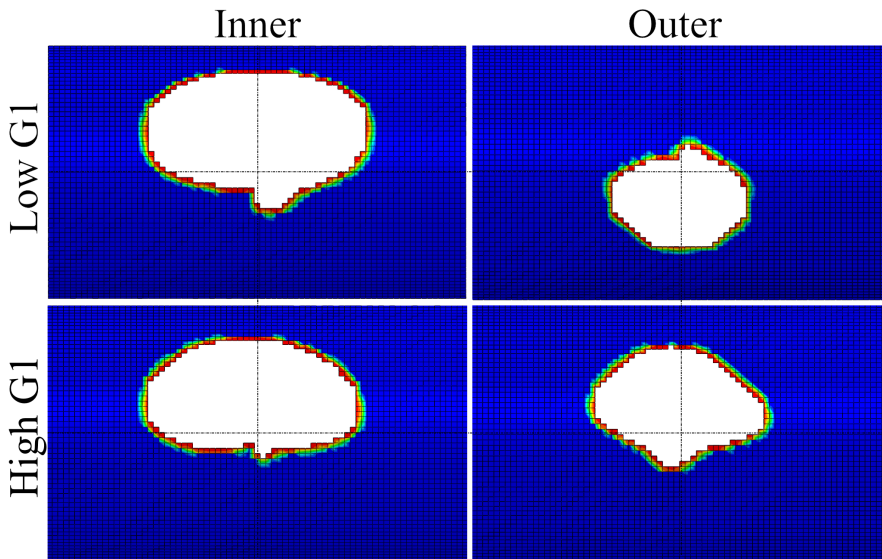


Figure 5.15: Delamination in inner and outer cohesive layer with adjusted G_{IC} . The colour of the elements represent the state of stiffness degradation. Blue elements are undamaged and red elements have high levels of damage. White region consists of deleted elements with no stiffness.

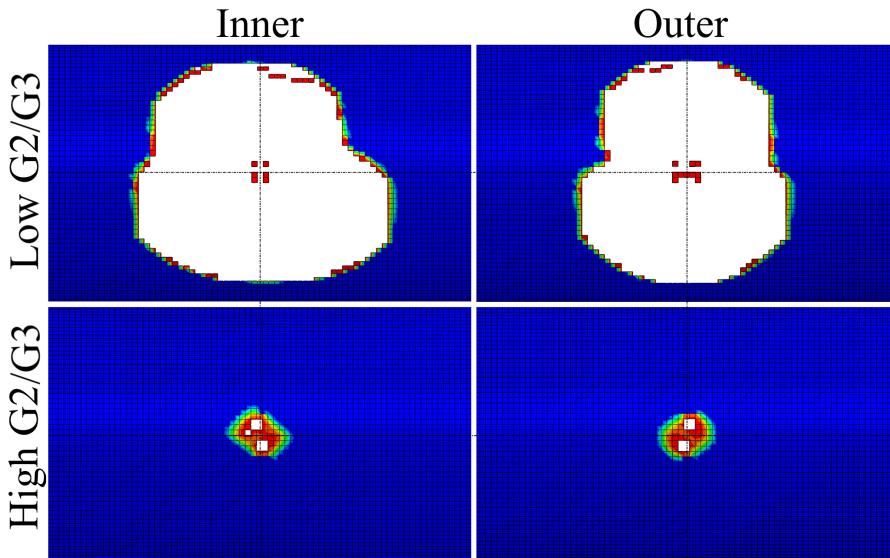


Figure 5.16: Delamination in inner and outer cohesive layer with adjusted G_{IIC}/G_{IIIC} . The colour of the elements represent the state of stiffness degradation. Blue elements are undamaged and red elements have high levels of damage. White region consists of deleted elements with no stiffness.

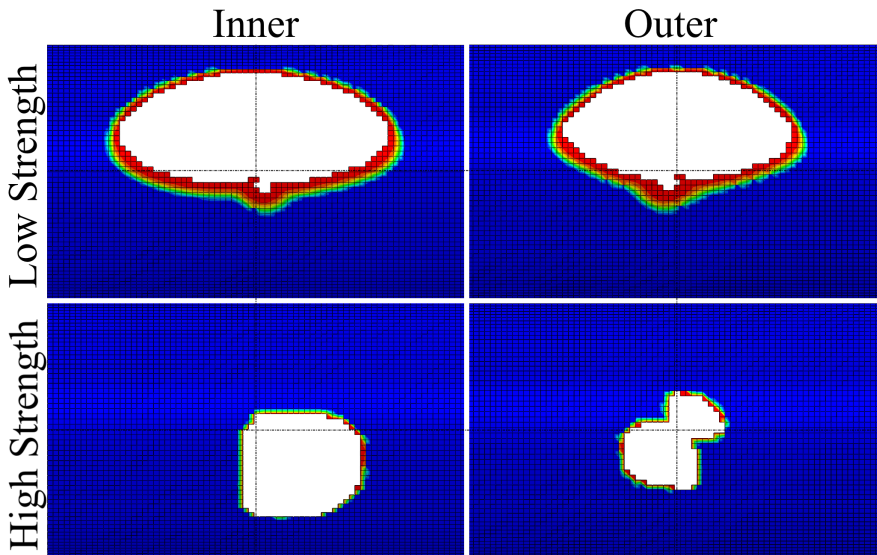


Figure 5.17: Delamination in inner and outer cohesive layer with adjusted tensile and shear failure stresses. The colour of the elements represent the state of stiffness degradation. Blue elements are undamaged and red elements have high levels of damage. White region consists of deleted elements with no stiffness.

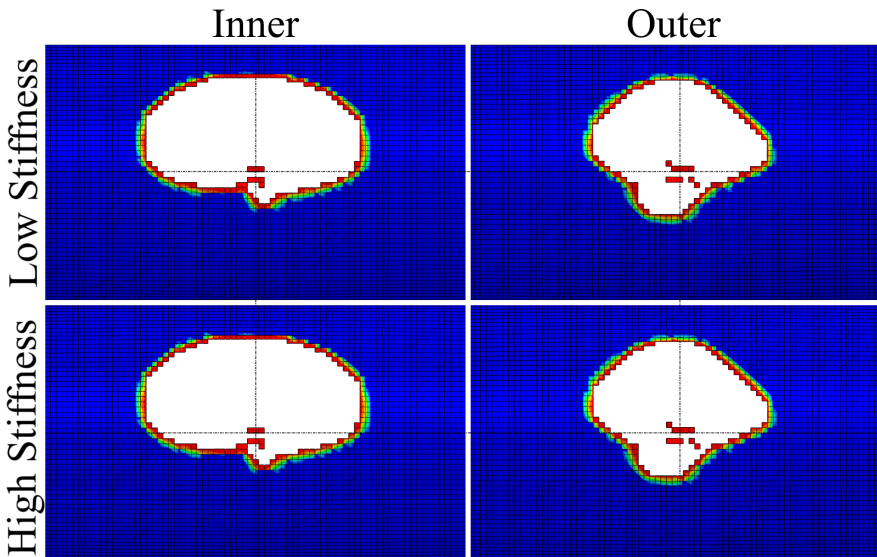


Figure 5.18: Delamination in inner and outer cohesive layer with adjusted tensile and shear stiffness. The colour of the elements represent the state of stiffness degradation. Blue elements are undamaged and red elements have high levels of damage. White region consists of deleted elements with no stiffness.

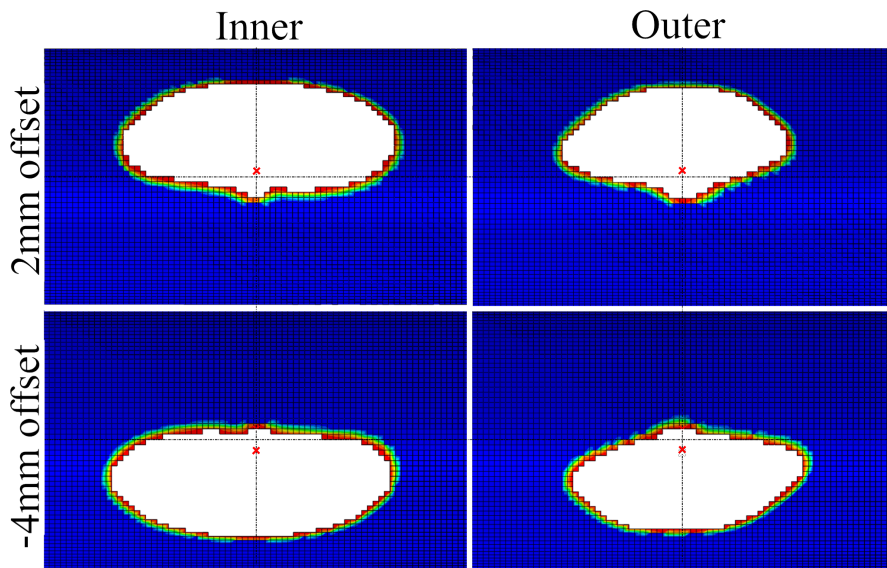


Figure 5.19: Delamination in inner and outer cohesive layer with adjusted impact location. The colour of the elements represent the state of stiffness degradation. Blue elements are undamaged and red elements have high levels of damage. White region consists of deleted elements with no stiffness.

5.2.5 Intralaminar damage

For the intralaminar damage, Hashin damage parameters were set according to Table 4.1. The following figures show numerical Hashin damage for a 1 m impact (see Figure 5.1 for the experimental damage). The delamination extends upwards for this case and can be seen in Figure 5.13.

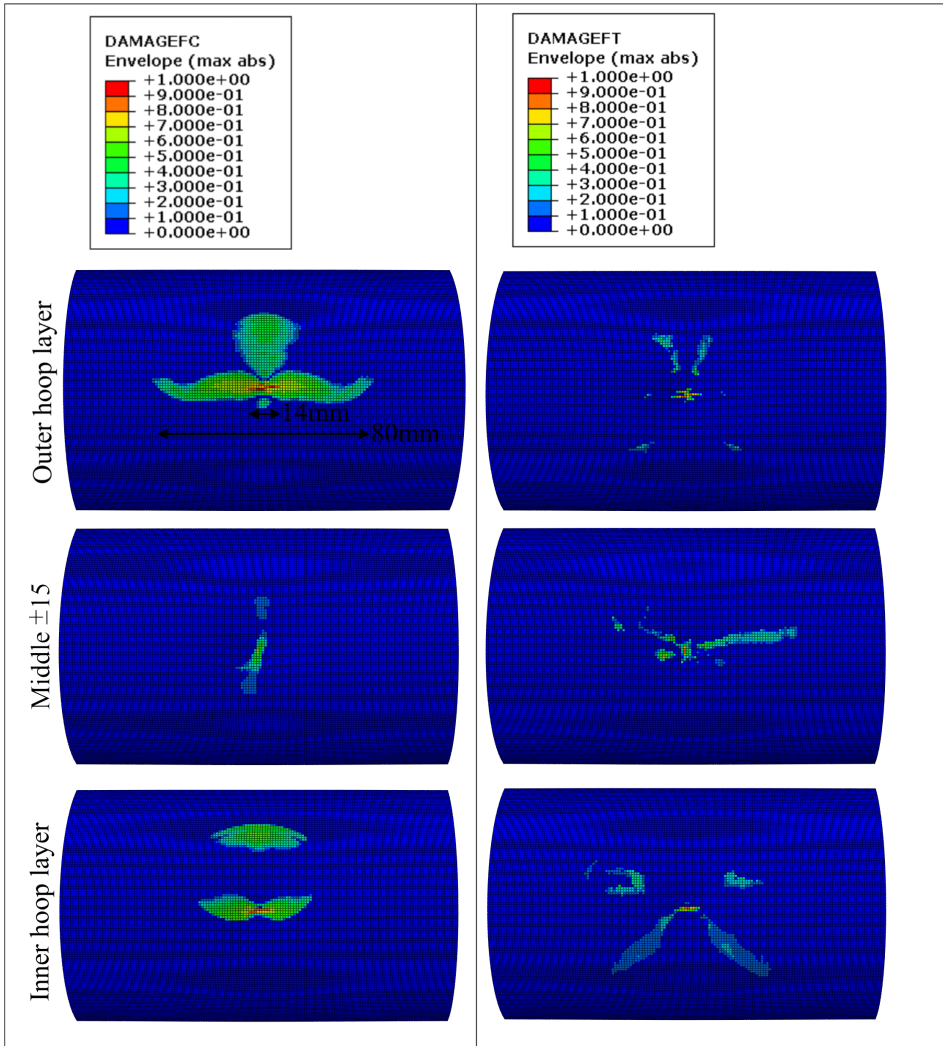


Figure 5.20: Fibre damage envelope. 1 m impact. The left side shows compression damage and the right side shows tension damage.

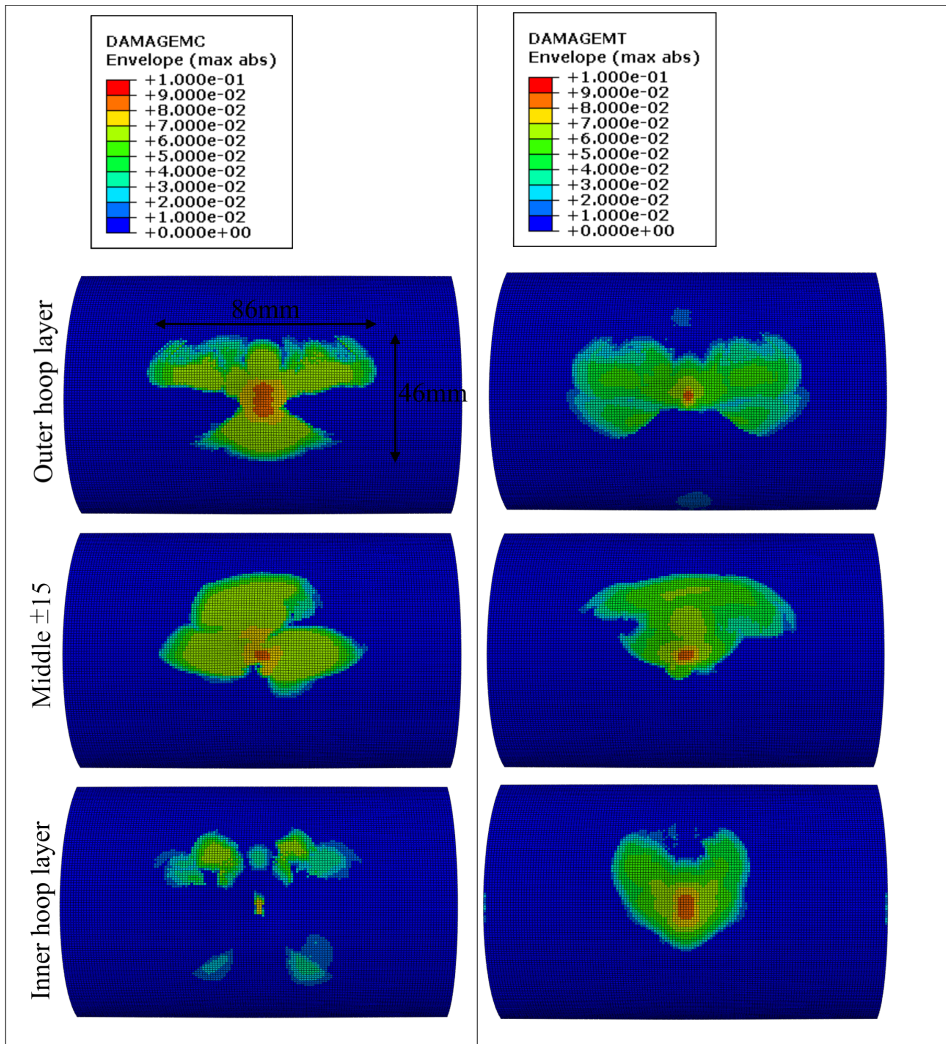


Figure 5.21: Matrix damage envelope. 1 m impact. The left side shows compression damage and the right side shows tension damage.

As seen in Figure 5.20, there is fibre damage to some extent in all layers. However, it is concentrated in the top layer, where many section points have reached full damage.

Figure 5.21 shows that the matrix damage covers a greater area than the fibre damage. However, the magnitude of the damage is a lot lower. This is due to the larger viscous damping employed to prevent zero shear stiffness.

Damage through section points

The shell approach simplifies the through thickness behaviour within a layer, since the in-plane strain will vary linearly even after the stiffness of the top section points have broken down. Figures 5.22 and 5.23 show the strain and stress distribution through section points 1 to 3 (bottom to top) for the element directly below the impactor. The strains and stresses were sampled at an arbitrarily chosen time after impact.

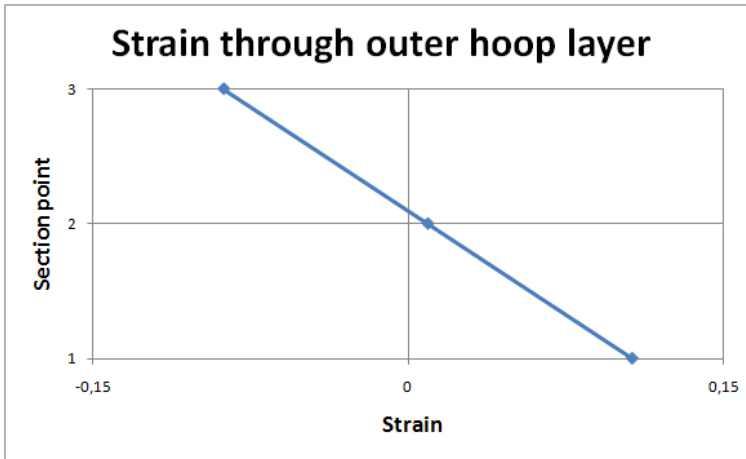


Figure 5.22: Strain through section points of top layer during impact. Element directly below impactor.

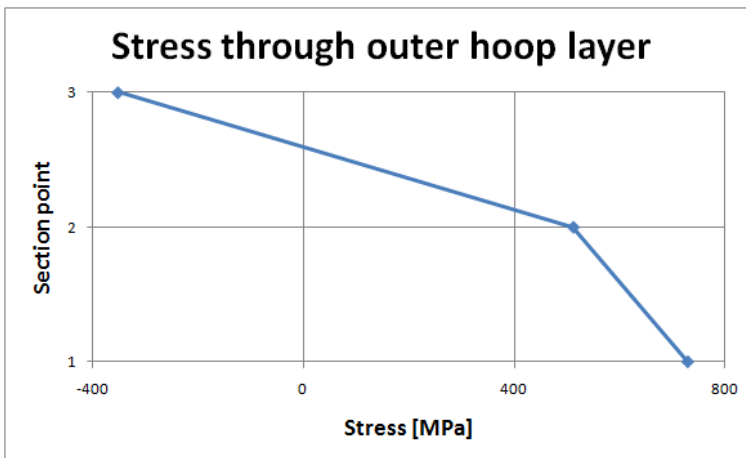


Figure 5.23: Stress through section points of top layer during impact. Element directly below impactor.

This simplification becomes apparent when looking at the distribution of damage through the section points of a layer. As Figure 5.24 shows, the impact caused total compressive damage for the line of elements below the impactor in the top section points of the top layer. For the middle and bottom section points however, there is almost no compressive damage below the impactor. For tensile damage, the bottom section point has some damage present below the point of impact.

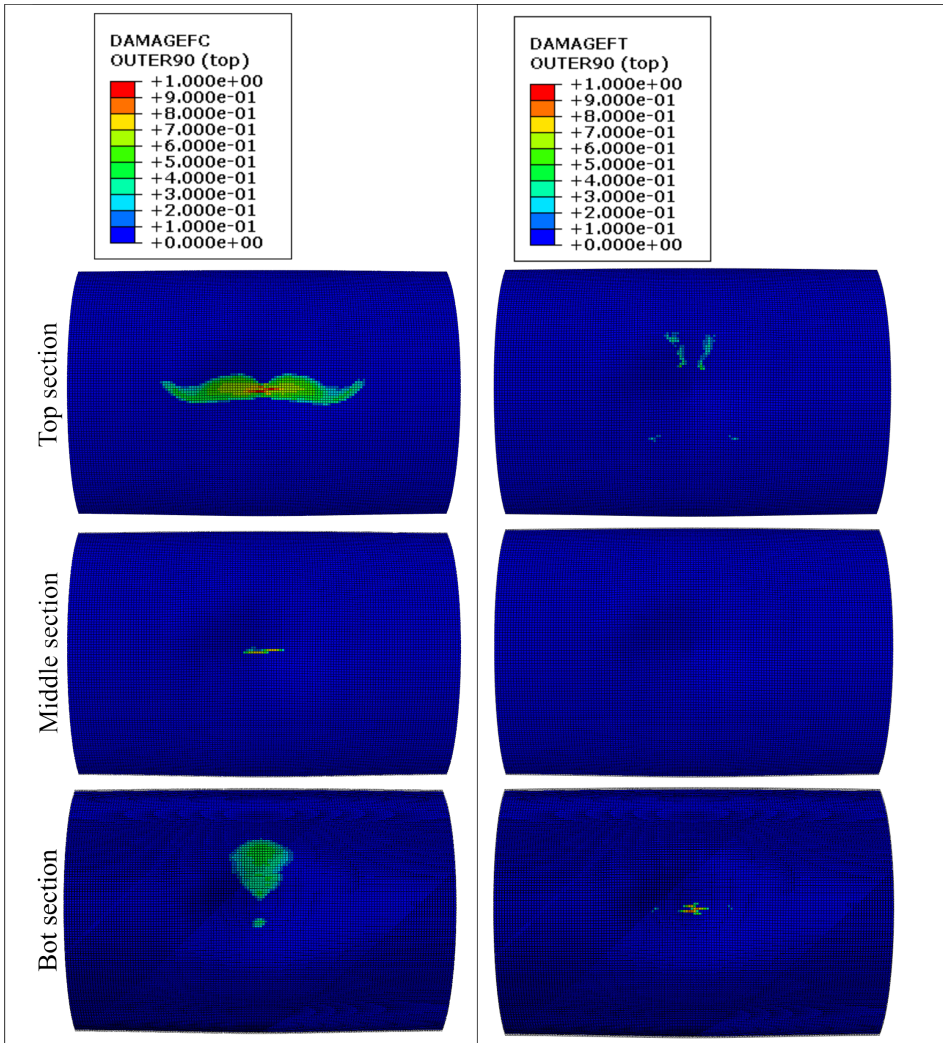


Figure 5.24: Tensile and compressive fibre damage through section points of top layer. 1 m impact. The left side shows compression damage and the right side shows tension damage.

Delamination damage correlation

The experimental impacts showed small scatter in both the size and shape of the delaminations. The asymmetric and elliptical shape was present in every specimen tested. This damage proved to be replicable within the Abaqus model when using suitable parameters. The delamination produced by both impact energies could be replicated by using the parameters from Table 4.1. As expected, the delamination was governed by shearing initially (Figure 5.10). After the damage evolved, a normal force was present in addition to the shear (Figure 5.11). Beforehand it was thought that the normal force and the accompanying G_{IC} was of little importance. However, as Figures 5.10 and 5.11 shows, the normal force cannot be neglected. The delamination sensitivity analysis (*Section 5.2.4*) also shows that G_{IC} is important to replicate the experimental delaminations, where a 50 % reduced value produces delaminations where the top and bottom interface have opposite directions. This indicates that the peeling of layers plays an important role, even in this scenario which is mostly shear based.

The asymmetry of the delaminations are an interesting phenomenon, as there was nothing in the model that favoured one side of the pipe apex over the other. In the experiment, local defects in the material, or small deviations in the location of impact etc. were sources for a preferred direction of delamination, but in the model none of these variations existed. However, the model was influenced by numerical round-off errors. This means that at points of structural instability, these small deviations could push the model one way or the other. This, combined with the local buckling of the pipe (Figure 5.9) provides a reasonable explanation for the asymmetry of the delamination. Additionally, it could be seen that opposing directions of delaminations was achieved by i.e changing G_{IC} for the cohesive sections (see Figure 5.15 compared to Figure 5.14). This strengthens the argument that the direction was governed by the randomness of the numerical round-off errors.

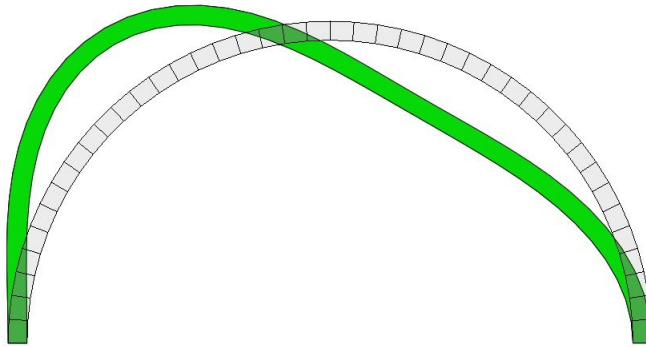


Figure 6.1: Buckling mode simulation of an arch.

As Figure 6.1 illustrates, the deflection of the pipe during impact is somewhat analogous to the buckling of an arch, and the direction of buckling seems to determine the direction of delamination. The buckling mode for the pipe is more complicated than in this simple arch, but the instability problem is similar. The thin laminate used had low bending stiffness, enabling large bending deformations and subsequent buckling during impact.

The sensitivity study showed that lowering the G_{IC} value by 50 % slightly reduced the size and altered the shape of the delamination. It also produced two separate directions of delamination for the inner and outer layer. Increasing it by 50 % had almost no discernible effect on neither the shape nor the size of the delamination. This indicates that setting the value too low can be critical, as the geometry of the damage was severely altered. However, having the value set too high did not seem to influence the results.

As expected G_{IIC}/G_{IIIC} had the most effect on the delamination. A 50 % reduction roughly doubled the area of the delaminations. It also removed almost all asymmetry. This may be caused by the delaminations propagating too quickly, reducing the stiffness before the "correct" buckling mode can be achieved. This makes it simply buckle in on itself rather than as in Figure 5.9. For the high G_{IIC}/G_{IIIC} value, the high energy required to create the fracture surfaces limited the delamination to almost nothing, as only a few elements dissipate enough energy to reach deletion.

Reducing the cohesive layer strength had virtually no effect. The shape and size of both delamination layers was perfectly conserved. However, the border between deleted and undamaged elements became a bit thicker. This can be explained by elements reaching the damage threshold sooner, but the damage evolution was relatively slower since the same energy needs to be dissipated prior to deleting the elements. When the strengths were increased the delaminations, were not consistent with the experimental results. Both shape and size was greatly altered. The mechanics behind this was not investigated. Suffice to say the strength needs to be set conservatively, or the results produced will not reflect the experimental damage.

Changing the stiffness of the cohesive layers did not have any effect on delamination in this

study. It can be explained by the relative thickness of the cohesive layers being very small, which makes the total response of the pipe virtually independent of the elastic behaviour of the cohesive zone. The model benefits from this, as the stiffness can be reduced if it becomes the limiting factor for the stable time increment.

Simulations using the impactor off-set from the apex of the pipe showed a connection between the side of delamination and the geometry of the deformation. The delamination followed the side of the impact in both cases. This strengthens the argument of buckling modes being critical when the delamination propagates. The buckling mode is determined by which side of the apex is impacted, and both cases presented delamination in the direction of the impact offset. The results also indicates that small deviations in impact locations does not alter the shape or size of delaminations. The experimental set-up benefits from this, as there is always some error in the impact location for the experiments.

The delaminations were accurately predicted when using the medium mesh. Using the medium mesh was possible since only the Hashin damage required the finest mesh, and Hashin damage was shown to not influence delamination (*Section 5.2.3*). Calculations for delamination took about 3 hours for a 10 ms impact. Some increased accuracy is achieved by using the fine mesh instead. However, this doubles the calculation time and results in very similar delaminations (Figure 4.11).

Delamination damage can cause a considerable reduction in strength, due to both local buckling of layers and the lost ability to carry shear through the cross section. For internal pressure such as in a pressure vessel, these delaminations does not have a great influence on the strength. However, good knowledge of the delamination caused by various impacts can serve as a means to identify the type and extent of damage. This may prove a valuable tool when determining the residual strength of impacted vessels.

Intralaminar damage correlation

For the intralaminar damage, the experimental results were inconsistent. Large cracks due to fibre compression were present in some samples but completely absent in others. The largest fibre crack was found in the batch of lowest impact energy. This indicates that the failure is closely linked to local material defects, and that these vary greatly within the same filament wound pipe. Therefore great care must be taken to select damage parameters that reflect the worst-case of material quality.

For the fibre failure, the burn-off tests and subsequent inspection of fibres revealed that fibre failure was limited to what was readily seen by the naked eye (Figure 3.7). The extent of fibre damage could therefore be accurately measured visually. For matrix cracking some large cracks near the impactor were visible both internally and externally for every sample. Additional matrix cracks were surely present, but the extent of these are unknown. The Hashin damage attempted to replicate the worst-case damage scenario (large fibre crack in 28.45 J impact, Figure 5.1). This was achieved by using Hashin parameters from Table 4.1.

As shown in Figure 5.20, the compressive damage propagated mostly in the top layer,

where a 14 mm line of elements reached total damage in their top section points. The elements were not deleted however, as only the top section points were totally damaged. The damage propagated longitudinally, which compares well to the experimental damage. The fibre damage extended 80 mm, where most of the damage had progressed less than 50 % ($d_f < 0.5$, less than 50 % stiffness reduction). For tensile damage, there was some damage in all layers, but nothing that had progressed beyond a few elements.

When comparing the numerical fibre damage to the experimental fibre damage, it could be seen that the damage within the area of the 30 mm crack (Figure 5.1) had reached 60 % in the model. When tweaking the model to represent the experimental damage, damage of 50 % or more was chosen to represent broke fibres. This was defined rather arbitrarily, since many comparisons between experimental and numerical damages would be needed to judge what damage level best reflects broken fibres.

Figure 5.21 shows that the matrix damage covers an area of roughly 86×46 mm for all layers. The matrix cracking that was seen in the experiment (Figures 5.3 and 5.1) is within the area predicted to contain matrix cracks. This area is larger than the area containing visible cracks in experiment, but cracks extend beyond what is visible to the naked eye. Determining the exact extent of the matrix damage was not attempted.

The tensile fibre damage present in the model was somewhat surprising, as the compressive strength is less than half the tensile strength. The reason for this lies within the simplifications of the shell approach, where all bending is about the neutral plane of the shell, even after the strength has deteriorated at i.e. the top section point. As Figures 5.22 and 5.23 show, the strain varies anti-symmetrically about the central section point, even after nearly all stiffness from the top section point is removed. This unrealistic bending deformation causes larger than realistic tensile stresses in the bottom section points of the damaged elements. It does not affect the overall behaviour much, as only a few of the section points have large degrees of damage. However, it heavily affects the propagation of damage through the thickness of elements. After the top section point has broken down in compression, the realistic scenario would be greatly increased compressive stresses in the middle section point. The artificial strain distribution from Figure 5.22 prevents this, which again caused the tensile damage in the bottom section points (Figure 5.24).

A possible solution to this problem is customizing the element deletion to remove elements after the top section point has reached a set amount of damage. Some problems due to instabilities might arise, but it would be necessary if serious amounts of fibre damage is to be predicted using shell elements. Using 3D elements in place of the continuum shell elements would also solve this, but it also prevents using the built-in Hashin damage in Abaqus, and would require implementing custom sub-routines for damage initiation and propagation.

The Hashin damage calculations were performed using the fine mesh. Since Figure 4.9 showed considerable differences between the mesh sizes. The calculation time for the Hashin simulations were therefore roughly 6 hours.

Ideally comparisons between numerical residual strength and experimental residual strength could be made based on i.e. experimental and numerical burst pressures or similar failure

tests. This was attempted but not achieved due to leakage problems when performing the experimental burst pressure tests.

Conclusion

The combined continuum shell and cohesive element model was able to predict delamination and fibre damage within the scatter of the experimental results. It is able to do so using well established damage criteria, enabling the models to be built with relative ease. The calculation time for meshes that capture both the shape and size of the damage is practical. For getting accurate delaminations, a mesh of 2×2 mm or finer in the damage zone was needed. At 2×2 mm calculation time was at roughly 3 hours (using 2 cores of Intel i5 2.6GHz). To accurately represent the evolution of fibre damage, a mesh of 1×1 mm was required. This resulted in calculation times of roughly 6 hours.

The experimental delaminations produced were consistent in shape, with some variation in size. All of the impacts caused asymmetric damage, veering from around the impactor to one side of the pipe apex. The asymmetry of the damage was well replicated by the model, despite nothing in the model itself causing this asymmetry. It is thought that the mechanism behind this is the local buckling mode of the pipe, triggered by slight numerical errors. For the experimental case, local defects and slight geometric imbalances are thought to determine the buckling direction, and therefore also the direction of delamination.

Initially the delamination is powered by the shear forces between layers exclusively. After the delamination has begun to develop, a wave of normal stress is present at the front of the delamination, which helps drive it further. As expected G_{IIC}/G_{IIIC} are the parameters that mostly influence the size of the delamination. However, the value of G_{IC} also plays a part in recreating the experimental delaminations numerically. The cohesive element strength yields a wider border of damaged elements between the undamaged and deleted elements when lowered, but the size and shape of the delamination is virtually unaffected. High strength yields unrealistic delaminations both in shape and size. The stiffness of the cohesive layers has very little influence on the delamination. Values can therefore be chosen to give a large stable time increment without affecting the results.

For the matrix and fibre damage the experiments had large scatter in results. The impacts

created large compressive cracks in the fibres for some samples, while no fibre damage was present in others. Matrix cracking was present both at the interior and exterior of the pipe. The larger matrix cracks near the impact location were readily seen by the naked eye, but the presence of many invisible cracks reaching far from the impacted region is nearly certain, as the strength of the matrix is very low. Burn-off tests verified that fibre damage was limited to the cracks which were easily seen.

The experiments showed that visible matrix damage was within the area predicted to contain matrix damage for the numerical model.

The fibre damage from the experiments could be reproduced by the numerical model, although the through thickness propagation in the layers was unrealistic due to the nature of the shell element approach. The large scatter in experimental fibre damage calls for larger sample sizes to determine the worst-case scenario. Different fibre damage geometries should ideally have been investigated to determine what damage level best corresponds to experimental fibre failure.

Overall it seems likely that this type of model can prove a valuable asset. Both to research the behaviour and mechanisms of damage as it is inflicted, as well as to predict the outcome of specific impacts, both in terms of delamination and fibre/matrix damage.

Further work

The model parameters used in this model provided good results for damage caused by a specific impactor geometry, at two different energy levels. Ideally the model is able to predict damage for a wide array of different impact geometries and energies. Further work is required to determine if the model is applicable to these different impact scenarios.

Residual strength tests to validate the state of fibre damage was planned for this thesis, through internal pressure tests. These were not accomplished due to technical problems with pressurisation. Testing that links the residual strength of the numerical model to experimental data would be of great value. Appendix A sums up the methods used and problems faced during the failed burst pressure tests. Hopefully this can be of aid if burst pressure tests are made by NTNU students in the future.

Bibliography

- [1] C Bouvet, B Castanié, M Bizeul, and J Barrau. Low velocity impact modelling in laminate composite panels with discrete interface elements. *International Journal of Solids and Structures*, 46(14):2809–2821, 2009.
- [2] JP Hou, N Petrinic, C Ruiz, and SR Hallett. Prediction of impact damage in composite plates. *Composites Science and Technology*, 60(2):273–281, 2000.
- [3] L Iannucci. Progressive failure modelling of woven carbon composite under impact. *International Journal of Impact Engineering*, 32(6):1013–1043, 2006.
- [4] HE Johnson, LA Louca, S Mouring, and AS Fallah. Modelling impact damage in marine composite panels. *International Journal of Impact Engineering*, 36(1):25–39, 2009.
- [5] C Menna, D Asprone, G Caprino, V Lopresto, and A Prota. Numerical simulation of impact tests on gfrp composite laminates. *International Journal of Impact Engineering*, 38(8):677–685, 2011.
- [6] G Perillo, NP Vedivik, and AT Echtermeyer. Damage development in stitch bonded gfrp composite plates under low velocity impact: Experimental and numerical results. *Journal of Composite Materials*, 49(5):601–615, 2015.
- [7] Z Changliang, R Mingfa, Z Wei, and C Haoran. Delamination prediction of composite filament wound vessel with metal liner under low velocity impact. *Composite Structures*, 75(1):387–392, 2006.
- [8] G Perillo. Numerical and experimental investigation of impact on filament wound glass reinforced epoxy pipe. 2014.
- [9] Z Hashin. Failure criteria for unidirectional fiber composites. *Journal of Applied Mechanics*, 47(2):329–334, 1980.

-
- [10] Abaqus 6.13. *Abaqus Analysis User's Guide*.
- [11] A Turon, C Davila, P Camanho, and J Costa. An engineering solution for mesh size effects in the simulation of delamination using cohesive zone models. *Engineering Fracture Mechanics*, 74(10):1665–1682, 2007.
- [12] 3B Fibreglass datasheet. <http://www.3b-fibreglass.com/hipertex/hiper-tex-performance-properties/>, 2015.
- [13] Hexion Epikure datasheet. <https://www.hexion.com/products/technicaldatasheet.aspx?id=8230>, 2015.
- [14] G Perillo. *Numerical and experimental investigation of impact behaviour of GFRP composites*. PhD thesis, NTNU, 2014.
- [15] G Perillo and AT Echtermeyer. Mode I fracture toughness testing of composite pipes. *Applied Composite Materials*, 20(6):1135–1146, 2013.
- [16] F Dharmawan, G Simpson, I Herszberg, and S John. Mixed mode fracture toughness of gfrp composites. *Composite Structures*, 75(1):328–338, 2006.
- [17] V Khentalov. Design and production of new end-fitting. Master's thesis, NTNU, 2015.

Appendix A: Burst pressure testing

A large number of pressure test were performed on both impacted and un-impacted composite pipes. Unfortunately none of these tests were able to burst the composite pipe. This is believed to be due to a combination of leaks in the liner and the liner/end-fitting interface. This chapter will describe the pressure tests conducted, different sealing methods attempted, the results and suggestions to improvement. These pressure tests have not contributed towards the overall goal for this thesis, however they are included to provide guidance for future pressure testing and residual strength testing. This is also in accordance with the latest urge in the scientific community to publish negative results to prevent others from conducting the same experiments.

The sealing problem

When subjecting the pipes to internal pressure, two main causes for leakage are present:

- Leakage between pipe and end-fitting
- Leakage through pipe matrix

The leakage between pipe and end-fitting is countered by a tight fit and an o-ring sealing the interface. However, the end-fitting was originally designed to leak before burst. Because of this the o-ring seal is broken by the bolt-holes in the pipe when the strain is sufficiently high.

The pipe itself is not completely water-tight, as tiny cracks in the matrix appear at very low stress. These cracks allow water to seep through at a low rate if no liner is used.

One of the problems when sealing the pipe is that the interior is not accessible after attaching the last end-fitting. This makes the sealing more difficult, as the method used needs to be performed before attaching the last end fitting.

Test setup

The pressurization tests were conducted by sealing each end of the composite pipe using metal end fittings produced by Anders Fossa in 2014. Various solutions were used to reduce seepage through the pipe. The pipe was then pressurized internally by a high pressure inlet in one of the end fittings, using a high pressure pump with 1000 Bar capacity. The pressure was logged using a digital manometer.

Liner methods attempted

No liner

Since the pump is able to supply a relatively large flow of water, the pressure is able to build up a considerable amount even with seepage through the matrix. With no sealing apart from the o-rings sealing the pipe/end-fitting interface, the pressure was able to build to 110Bar. At this pressure the pump was suddenly unable to supply enough flow to overcome the leakage. The leakage at this point was mainly through the end-fitting interface, where the longitudinal forces pulled the bolt-holes of the pipe onto the o-ring. The pipe used was roughly 3mm thick, with an additional $\pm 45^\circ$ layer reinforcing the ends.

Rubber Balloon

An attempt was made to seal the pipe by using a balloon, attached to a machined pressure nipple at the interior of end fitting. Unfortunately the balloon burst before reaching high pressures, rendering the method useless. It is still thought to be one of the more promising solutions, as it can be easily assembled before attaching the end-fittings. However, a very robust balloon needs to be used, as there is considerable movement between the pipe and the end-fitting during pressurisation.

Plastic foil

Thick plastic foil attached to the interior of the pipe with sticky-tape was attempted both to seal the seepage through the matrix, and to alleviate some of the leakage through the pipe/end-fitting interface. The method proved effective when it was used to stop the locally large leakage at points of impacts, where it was able to form a tight seal and stopping the local leakage. When sealing the interface between the pipe and end-fitting, it was not as effective. The end which was accessible from the outside before attaching the last end-fitting was able to provide an adequate seal. The last end-fitting interface was not accessible from the outside, and therefore a good seal was not achieved.

PET pipe

Using a PET pipe as a liner provided a robust seal preventing leakage from the pipe through the matrix. It also enabled additional sealing of the pipe/end-fitting interface by sealing the interface between the PET-pipe and the end-fitting with sticky-tape, prior to attaching the end-fittings. However, the same problem with leakage through the end fitting interface presented itself. As the pressure increases a gap between the PET-pipe and the end fitting appears. This breaks the seal of the liner, and leakage occurs.

End-fitting interface

To prevent the excessive leakage through the end-fitting interfaces, sealing them with sticky tape before attaching the pipes to the end fittings was attempted. This did help somewhat with the leakage, but given enough pressure also this method failed to provide an adequate seal.

Discussion of results

The tests conducted showed that even with no liner or extra sealing the pressure is able to reach 110Bar before the rate of leakage exceeds the pumps capacity. At this pressure the limiting factor is the pull-out of the end fittings. By having thicker reinforcements of the pipe at the ends, this pressure can likely be increased somewhat. However, the geometry of the end fitting makes it so that it can only be reinforced to a thickness of 5mm. Therefore it is unlikely pressures far exceeding 110Bar is achievable without a good seal.

None of the attempts to seal the pipe were able to overcome both the problem with seeping through the matrix and the leakage through the pipe/end-fitting interface. Eventually the large strains managed to break all the sealing techniques. The most promising approach is thought to be the balloon approach, but using a much thicker and flexible balloon than what we attempted. This due to the large movements of the parts being supported by the flexible balloon.

Recommendation for future work

For future attempts to reach burst pressure the following recommendations are made:

- Use new end fitting not designed to leak before burst.
- Use end-dome with pressure inlet to wind a tank which can be directly pressurised.

A new end fitting is currently being developed by Vadim Khentalov[17]. This end fitting is not designed to leak before failure, so the movement of the end fitting is not as critical. Additionally it supports thicker pipes, meaning the pipe ends can be reinforced further, making the tear out of bolt-holes less prominent.

Alternatively, omitting the end-fittings altogether, and instead winding onto domes with a pressure inlet and a liner allows for a very promising seal. The disadvantage being that only one specimen can be wound at a time.

Appendix B: Winding procedure

Preparations

Before starting the winding procedure, the mandrel was thoroughly cleaned with acetone, before it was coated in 2 layers of **FlexZ Z3.0** Slipcoat system and one final layer off **RENLEASE QV5110** slip wax. It proved important to apply a thick layer of wax onto the parts of the domes that were inserted into the mandrel(Figure 8.1). If not properly sealed in this fashion, epoxy will get into the interface between the parts, and extracting them will be difficult.

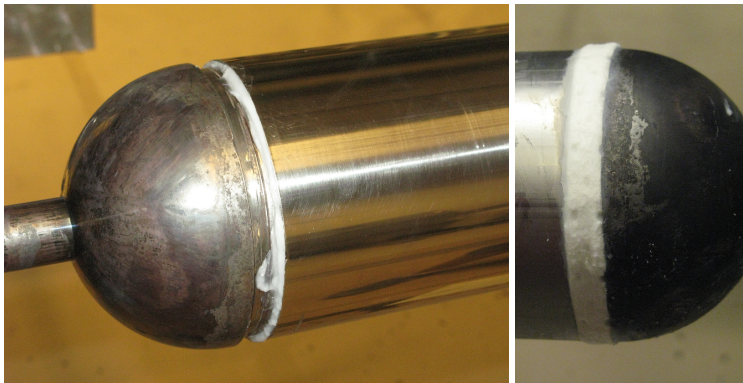


Figure 8.1: Wax applied between end dome and mandrel, breather soaked in wax is then wound into groove.

To get a smooth surface over the grooves in the end domes and to further improve the seal, breather fabric was cut to the correct size, soaked in wax and wound into the groove.

The pipe was mounted in the machine, and the length from each of the two grooves were measured from a fixed reference point (this is important since after winding, finding the grooves into which you want to cut can be difficult). The distance between the chuck and the top of the first dome also needs to be measured, as this offset needs to be specified in the programs, in order for the machine to know where to start winding. This is important to get right, as errors here can cause the machine to collide into itself.

The winding process was started by pulling the fibre through until the wetted part reached the mandrel, winding it a few rounds by hand, and then taping it to the central axle of the mandrel (Figure 8.2).

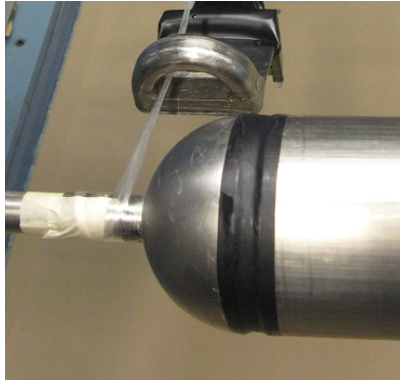


Figure 8.2: Fibre attachment before winding.

The Winding process

Our pipe was wound with both helical and hoop layers. This gives us transitions in the winding process where steps need to be taken to make sure the fibre orientates itself correctly.

The first transition is at the very beginning, when the fibre that is wound around the axle needs to reach the top of the dome where the hoop program begins. Since the dome is very steep, and the fibre very slippery, it won't easily follow the movements of the machine.

The solution for this was to manually traverse the eye to the starting position, applying a few rounds of rotations while guiding the fibre to the top of the dome. After the fibre had been wound on top of itself a few times, there was enough friction to hold the fibre in place. The hoop program could then be started.

When going from helical to hoop layers, the transition is especially troublesome. The fibre will immediately start on the low angle helical winding after finishing the hoop. This means that the fibre will go from an angle of 90° to an angle of $\approx 15^\circ$. There is not enough friction to support this, and because of that the fibre from the hoop layer will get pulled along by the helical winding (Figure 8.3).

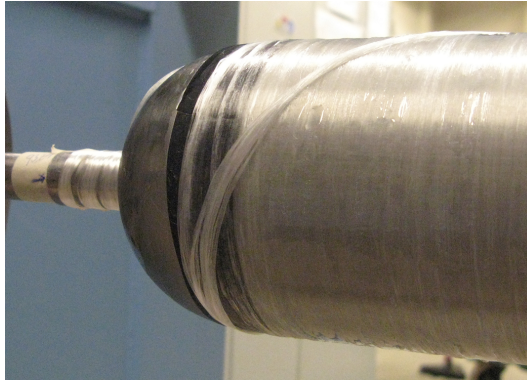


Figure 8.3: Fibre pulled downward by helical layer transition.

To counteract this effect, a similar approach as for the start was taken. During the transition, the speed of the machine was turned low, and the fibre was held in place at the edge of the dome by hand. This needed to be held tightly for a few rotations, until the fibre was held in place by the fibres wound on top of it. The path of the fibre where held in place deviated by a small amount, but it quickly assumed its correct path. This method was quick and easy, albeit a bit messy.

For the last transition, when going from helical to hoop, the problem is the same as when starting the winding process. The fibre needs to traverse the dome, and place itself neatly onto the mandrel. This was solved in the same manner as for the first hoop layer (Figure 8.4).

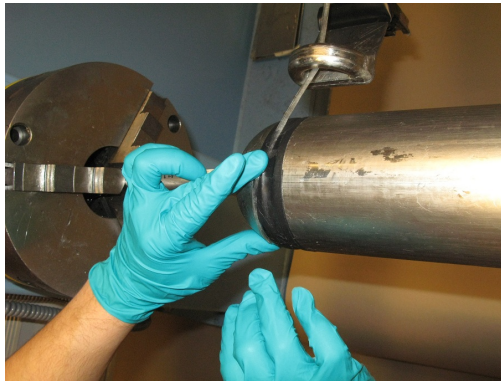


Figure 8.4: Fibre manually held in place so it doesn't slip off dome.

The CNC winding commander software has an option where you can insert transition layers. These are however only good for transitioning between one helical layer to another. It is simply a layer with very low coverage, where the fibre angle is changed gradually. Angles high enough to enable hoop winding without slipping are not available

however.

An alternative method to the transitions could be cutting the fibre and manually winding the start of each layer. This was not done however, as simply holding the fibre in place provided adequate results.

After winding

After winding, the mandrel needs to rotate for 24 hours, to ensure even distribution of epoxy as it cures. This is also a good opportunity to remove excess epoxy manually. It was not done for our pipes, and as a result, a thin layer of excess epoxy remained on the outside of both pipes.

It is also important to remember to clean the machine before the epoxy hardens.

After the 24 hours of curing in room temperature, the mandrel and pipe was placed in an oven at 80°C for 8 hours.

Pipe extraction

When the pipe was done curing, it was mounted back into the machine, and the grooves located by using the measurements taken earlier. A fein saw was used to cut the pipe at the grooves. This was attempted both by hand and by attaching it to the machine. Doing it by hand while rotating the mandrel in the machine proved to be the quickest and easiest solution.

The first end dome was removed by threading a thick metal cylinder onto the axle, and attaching a simple end fixture at the end by using the M8 threads. The metal cylinder is then knocked against the end fixture to remove the dome.

The remaining dome is removed by inserting a steel rod and knocking it out from the inside.

To remove the pipe from the mandrel, the mandrel was pushed and pulled out using the jig in Figure 8.5.



Figure 8.5: Jig for separating pipe from mandrel.

The first few centimetres are pushed through by using a jack. This requires a great deal of force to overcome the static friction, and to break apart the wax connecting the pipe to the mandrel. After initially pushing the mandrel, a heavy strap is thread through the pipe, and the mandrel is then pulled through by using a heavy duty lifting jack. The strap is fixed to the pipe by using a metal end plate that only covers the mandrel (Figure 8.6).



Figure 8.6: Strap is secured to the plate, then pulled through.

To protect the polished mandrel, tape was applied to the hole in the jig. This was not sufficient, as the pipe quickly rips multiple layers of tape apart. A better solution proved to be using both tape, and some rags to keep the steel mandrel away from the jig.

The glass fibre was removed from the end domes by burn-off at 600°C for 5 hours. This produced some minor oxidation at the surface. Next time a somewhat lower temperature will be used for burn-off.

NTNU		Kartlegging av risikofylt aktivitet		Utarbeidet av		Nummer		Dato	
HMS				HMS-avd.		HMSRV2801		22.03.2011	
				Godkjent av				Erfatter	
				Rektor				01.12.2005	

Dato: 24.02.2015

Enhet: Andreas Echtermeyer

Linjeleder: Andreas Echtermeyer

Deltakere ved kartleggingen (m/ funksjon): Martin Welle Skaar, Andreas Echtermeyer


(Ansv. veileder, student, evt. medveiledere, evt. andre m. kompetanse)

Kort beskrivelse av hovedaktivitet/hovedprosess: Prosjektoppgave student Martin Welle Skaar. Tittel på oppgaven: Modeling and testing

of impact damage in composite pressure vessels.

Er oppgaven rent teoretisk? (JA/NEI): Nei

risikovurdering. Dersom «JA»: Beskriv kort aktiviteten i kartleggingskjøremøet under. Risikovurdering trenger ikke å fylles ut.

Signaturer: Ansvarlig veileder: 

Student: Martin W. Skaar

«JA» betyr at veileder inneslår for at oppgaven ikke inneholder noen aktiviteter som krever

ID nr.	Aktivitet/prosess	Ansvarlig	Eksisterende dokumentasjon	Eksisterende sikringstiltak	Lov, forskrift o.l.	Kommentar
1	FEM analyser på PC	Martin Welle Skaar				Teoretisk
2	Oppgaveskriving	Martin Welle Skaar				Teoretisk
3	Vikling av rør med "Filament Winding" maskinen	Martin Welle Skaar	"Filament Winding" kurs, brukermanual	Obligatorisk opplæring, HMS kurs, verneutstyr, sensorer for nødstop		
4	Testing av rør	Martin Welle Skaar		Obligatorisk opplæring, HMS kurs, verneutstyr		
5	Trykktesting av rør	Martin Welle Skaar		Obligatorisk opplæring, HMS kurs, verneutstyr		

NTNU		Risikovurdering		Utarbeidet av		Nummer		Dato	
				HMS-avd.		HMSRV2601		ZZ.03.2011	
				Godkjent av		Rektor		Erstatter	
								01.12.2006	

Enhet:


Dato: 24.02.2015

Linjeleder: Andreas Echetermeyer

Deftakere ved kartleggingen (m/ funksjon): Martin Welle Skaar, Andreas Echetermeyer

(Ansv. Veileder, student, evt. medveiledere, evt. andre m. kompetanse)

Risikovurderingen gjelder hovedaktivitet: Prosjektoppgave student Martin Welle Skaar. Tittel på oppgaven: Modeling and testing of impact damage in composite pressure vessels.

Signaturer:  Ansvarlig veileder.

Student: *Martin W. Skaar*

ID nr	Aktivitet fra kartleggings-skjemaet	Mulig uønsket hendelse/ belastning	Vurdering av sannsynlighet (1-5)	Vurdering av konsekvens:				Risiko-Verdi (menneske)	Kommentarer/status Forslag til tiltak
				Menneske (A-E)	Ytre miljø (A-E)	ØK/ materiel (A-E)	Om-dømme (A-E)		
1	FEM analyser på PC	PC-Fatigue	1	B				1B	Teoretisk
2	Oppgaveskriving	PC-Fatigue	1	B				1B	Teoretisk
3A	Vikling av rør med "Fillament Winding" maskinen	Klemmskader og andre skader i kontakt med maskinen	1	D				1C	Verneutstyr, riktig bruk av sensorer, bruk i henhold til opplæring/manual
3B		Søl av kjemikalier på hud	3	B				3B	Verneutstyr, orden på laben
3C		Søl av kjemikalier på øyne	1	D				1D	Vernebriller, orden på laben
3D		Søl av kjemikalier på klær	3	A		A		3A	Verneutstyr, orden på laben
3E		Søl av kjemikalier på utstyr og gulv	3		C			3C	Tildekking av utstyr og gulv, orden på laben
3F		Mekanisk skade på utstyr	2		C			2C	
4A	Testing	Klemmskader og andre skader i kontakt med maskinen	2	C				3C	Verneutstyr
4B		Øyeskader fra splinter	1	D				1D	Vernebriller
4C		Mekanisk skade på utstyr	2		C			2C	Bruk i henhold til opplæring/manual
5A	Trykktesting av rør	Skade pga vannsprut	2	B				2B	Tildekking av rør, verneutstyr.

THE NORWEGIAN UNIVERSITY
OF SCIENCE AND TECHNOLOGY
DEPARTMENT OF ENGINEERING DESIGN
AND MATERIALS

**MASTER THESIS SPRING 2015
FOR
STUD. TECHN. MARTIN WELLE SKAAR**

Modeling and Testing of Impact Damage in Composite Pressure Vessels

Composite pressure vessels are becoming widely used for transporting gas and lately also hydrogen. In order to enable extensive use of the pressure vessels, it is of primary importance to ensure their societal acceptance and thus safety under transportation must be secured. In particular, the knowledge on composite overwrapped pressure vessels' (COPV) behavior when submitted to mechanical impacts is limited and existing standards are not well-appropriate to composite materials.

The main objective of this master thesis is to expose composite pressure vessels to well defined impact damage and to model their response with finite element analysis. Experiments shall be made on representative model structure to validate and improve the modeling approach.


Formal requirements:

Three weeks after start of the thesis work, an A3 sheet illustrating the work is to be handed in. A template for this presentation is available on the IPM's web site under the menu "Masteroppgave" (<http://www.ntnu.no/ipm/masteroppgave>). This sheet should be updated one week before the master's thesis is submitted.

Risk assessment of experimental activities shall always be performed. Experimental work defined in the problem description shall be planned and risk assessed up-front and within 3 weeks after receiving the problem text. Any specific experimental activities which are not properly covered by the general risk assessment shall be particularly assessed before performing the experimental work. Risk assessments should be signed by the supervisor and copies shall be included in the appendix of the thesis.

The thesis should include the signed problem text, and be written as a research report with summary both in English and Norwegian, conclusion, literature references, table of contents, etc. During preparation of the text, the candidate should make efforts to create a well arranged and well written report. To ease the evaluation of the thesis, it is important to cross-reference text, tables and figures. For evaluation of the work a thorough discussion of results is appreciated.

The thesis shall be submitted electronically via DAIM, NTNU's system for Digital Archiving and Submission of Master's theses.


Torgeir Welo
Head of Division


Andreas Echtermeyer
Professor/Supervisor

 NTNU
Norges teknisk-
naturvitenskapelige universitet
Institutt for produktutvikling
og materialer